Interpretation and processing of ASTER data for geological mapping and granitoids detection in the Saghro massif (eastern Anti-Atlas, Morocco)

Matteo Massironi*
Luca Bertoldi
Paolo Calafa
Dario Visonà
Dipartimento di Geoscienze, Università degli Studi di Padova, via Giotto 1, 35137 Padova, Italy

Andrea Bistacchi
Dipartimento di Scienze Geologiche e Geotecnologiche, Università degli Studi di Milano-Bicocca, Italy

Claudia Giardino
CNR-IREA (Italian National Research Council–Istituto per il Rilevamento Elettromagnetico dell'Ambiente), Milano, Italy

Alessio Schiavo
Land Technologies and Services (LTS) Srl., Treviso, Italy

ABSTRACT

Satellite remote sensing analysis is extensively used for geological mapping in arid regions. However, it is not considered readily applicable to the mapping of metamorphic and igneous terrains, where lithological contacts are less predictable. In this work, ASTER (Advanced Spaceborne Thermal Emission and Reflection Radiometer) data were used to clarify the geological framework of the Precambrian basement in the Saghro massif (eastern Anti-Atlas, Morocco). The Saghro basement is composed of low-grade metasedimentary sequences of the Saghro Group (Cryogenian), intruded by calc-alkaline plutons of late Cryogenian age. These rocks are unconformably covered by volcanic to volcaniclastic series of Ediacaran age that are broadly coeval with granitoid plutons. All of these units are cut by a complex network of faults associated with hydrothermal fluid flows, which developed during and shortly after the emplacement of the volcanic rocks. The geological mapping of the Precambrian units was challenging in particular for the Edicaran granitoid bodies, because they are characterized by very similar compositions and a widespread desert varnish coating. For this reason, a two-stage approach has been adopted. In the first step, false color composites, band ratios, and principal components analyses on visible and near infrared (VNIR) and shortwave infrared (SWIR) bands were chosen and interpreted on the basis of the field and petrographic knowledge of the lithologies in order to detect major lithological contacts and mineralized faults. In the second step, a major effort was dedicated to the detection of granitoid plutons using both thermal infrared (TIR) and VNIR/SWIR data. The ASTER TIR bands were used to evaluate Reststrahlen and Christiansen effects in the granitoid rocks spectra, whereas VNIR/SWIR false color composite and ratio images were chosen directly on the basis of the granitoid spectra (derived from both spectrophotometric analyses of samples and selected sites in the ASTER image). Finally, spectral angle mapper (SAM) and supervised maximum-likelihood classifications (MLL) were carried out on VNIR/SWIR data, mainly to evaluate their potential for discriminating granitoid rocks.

The results have further demonstrated the value of ASTER data for geological mapping of basement units, particularly if the processing has been based on a detailed knowledge of the rock mineral assemblages. In addition, the analytical comparison of ASTER TIR and VNIR/SWIR data has demonstrated that the latter are very effective in the distinction of granitoids with very similar silica content, because they can be recognized by secondary effects related to their hydrothermal and surface alterations (K-feldspar kaolinitization, plagioclase saussiritization, substitution of mafic minerals with oxides, inhomogeneous desert varnish coating, and clay/oxide proportions).

Keywords: Remote sensing, geological mapping, granitoid rocks, Precambrian basement, Anti-Atlas.

INTRODUCTION

Remote sensing by satellite images is frequently used for geological mapping in desert or semiarid lands, and numerous excellent results have been obtained for sedimentary sequences using Landsat data (Sgavetti et al., 1995; Lang, 1999, and references therein). In contrast, satellite remote sensing is not considered to be readily applicable to the mapping of metamorphic and igneous sequences because in such rocks, lithological contacts are less predictable, spectral features less defined, and thermal bands, sensitive to Si-O bonds, may lack adequate spatial resolution. Nevertheless, some outstanding results were recently obtained for such rocks using ASTER (Advanced Spaceborne Thermal Emission and Reflection Radiometer) and hyperspectral (e.g., Airborne Visible/Infrared Imaging Spectrometer) data in mineral mapping projects (Rowan et al., 2000, 2003, 2005, 2006; Rowan and Mars, 2003; Hubbard and Crowley,

*matteo.massironi@unipd.it

Geosphere; August 2008; v. 4; no. 4; p. 736–759; doi: 10.1130/GES00161.1; 18 figures; 3 tables.

2005; Mars and Rowan, 2006; Van Ruitenbeek et al., 2006, Hubbard et al., 2007). However, the detection of lithological or tectonic contacts, implying the detailed recognition of individual lithological units, is rarely attempted (Longhi et al., 2001; Watts et al., 2005).

In this work, begun within the Saghro basement geological mapping project (2003–2005) (Massironi et al., 2007; Dal Piaz et al., 2007; Schiavo et al., 2007; El Boukhari et al., 2007) and continued afterward, ASTER-derived products were tested for mapping various metasedimentary, intrusive, and volcanic units. In particular, geological mapping of the Precambrian Saghro massif, composed of turbiditic metasediments and magmatic rocks, was achieved through integration of multispectral remote sensing analysis, petrographic studies, and field observations. The remote sensing processing and interpretation was subdivided into two steps. During the first phase, false color composites, band ratios, and principal components analysis were applied to visible and near infrared and shortwave infrared (VNIR/SWIR) data to detect major lithological contacts and mineralized fault veins; the second step, based on both thermal infrared (TIR) and VNIR/SWIR data, was mainly focused on the recognition of diachronous granitoid bodies with very similar compositions.

GEOLOGICAL FRAMEWORK

The Precambrian Anti-Atlas belt developed during the Pan-African orogeny, when the West African craton collided with the northern active continental margin (Saquaque et al., 1989; Hefferan et al., 1992, 2002; Ennih and Liégeois, 2001). Remnants of subducted oceanic lithosphere are preserved as a discontinuous ophiolitic suture (Bou Azzer and Sirwa massifs) along the Anti-Atlas major fault (Leblanc and Lancelot, 1980; Saquaque et al., 1989; Hefferan et al., 1992; El Boukhari et al., 1992).

The eastern Anti-Atlas includes the Jebel Saghro and Ougnat basement massifs, where Precambrian rocks crop out below the discordant Paleozoic to Mesozoic sedimentary cover (Fig. 1).

The Jebel Saghro massif is composed of Cryogenian metaturbiditic sequences interleaved with a few basalt flows (Saghro Group of Thomas et al., 2004). The metaturbidites are intruded and overlain by two magmatic suites

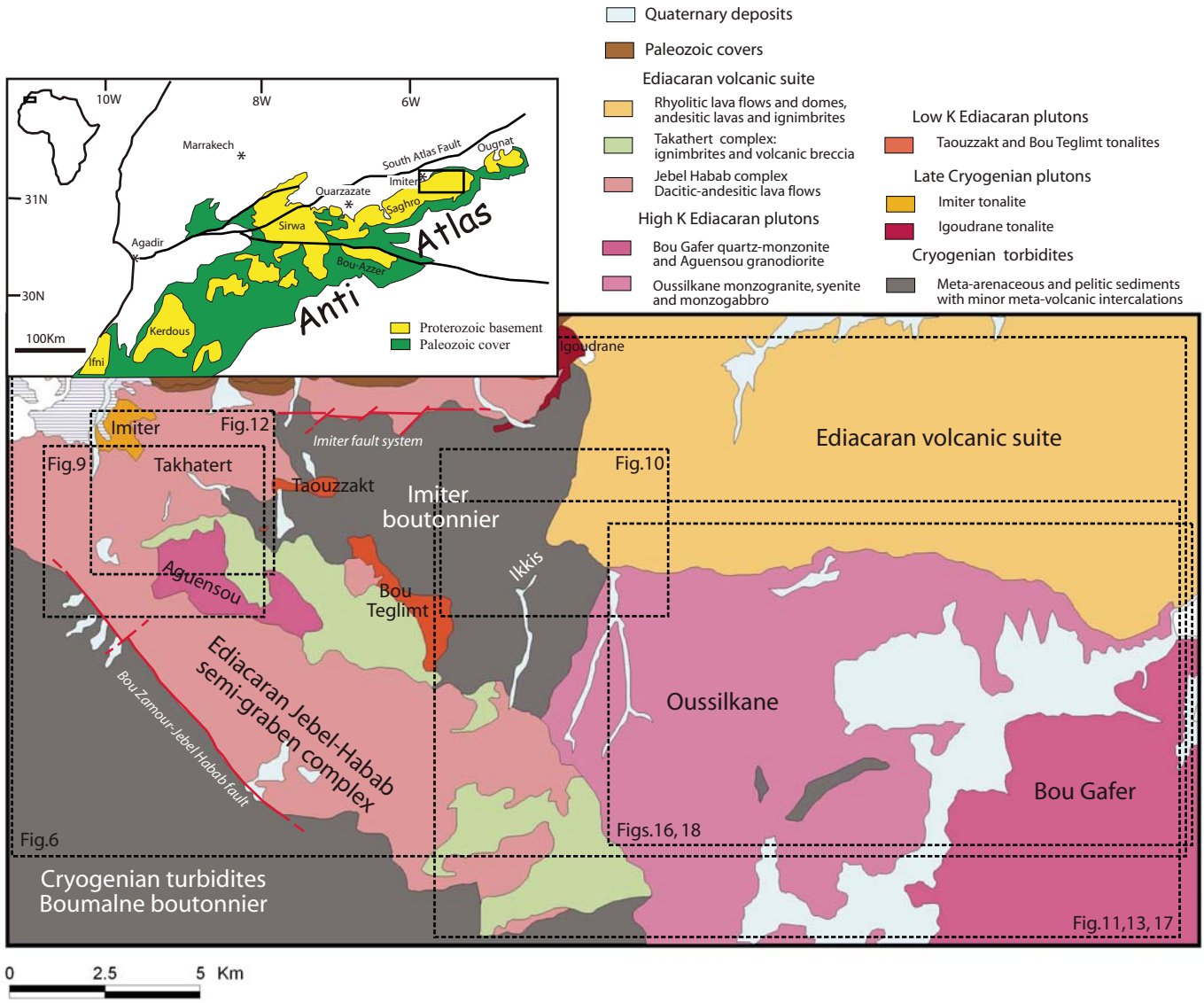

Figure 1. Geological sketch map of the Saghro area (modified after Hinderemeyer et al., 1977). Inset shows the Anti-Atlas belts.

related to the Pan-African volcanic arc (Ouarzazate Supergroup; Saquaque et al., 1992; Hefferan et al., 2000; Thomas et al., 2004; Fig. 1). The older suite is composed of calc-alkaline trondhjemitic intrusives (late Cryogenian), that in turn were exhumed and unconformably overlain by a younger magmatic suite composed of volcanic and volcaniclastic series (Ouarzazate Group) associated with broadly coeval plutonic to subvolcanic bodies with a low-K to high-K calc-alkaline composition (Ediacaran; Fig. 1).

The topography of the Saghro massif is characterized by some cliffs 2000–2100 m above undulating plateau areas ranging between 1650 and 1900 m in elevation. The higher reliefs are generally formed by thick volcanic and volcaniclastic sequences, whereas the metaturbidites and most of the plutonic bodies are confined to plateau areas. However, some plutonic bodies (Taouzzakt, Bou Teglimt, Arharrhiz) may constitute important exceptions, with peaks reaching 2000 m in elevation. In the following, the most important units are described from petrographic, stratigraphic, and structural points of view.

Saghro Group

Cryogenian metasediments

The lower Neoproterozoic turbiditic deposits consist of low-grade (greenschist facies), fine- to medium-grained metasediments, mainly represented by biotite-rich phyllites to metasandstones with centimetric biotite, sericite, quartz, and graphite layers with various amounts of plagioclase and quartz phenoclasts (Fig. 2A). Dikes, sills, and flows of metamorphosed picrobasalts occur locally (Fekkak et al., 2001). The metasediments crop out in the Imiter and Boumalne "boutouniers" (as defined by Choubert, 1945, 1952), and were regionally folded during the Pan-African syncollision event involving ductile deformation (Ighid et al., 1989; Ouguir et al., 1994; Saquaque et al., 1992).

Ouarzazate Supergroup

Late Cryogenian plutons

Two Cryogenian age plutons, the Imider and Tiboulkhirine, occur in the area. The Imider pluton has usually been attributed to the Eburnean (Hinderemeyer et al., 1977), but from the stratigraphic position (below the Ouarzazate basal conglomerates; Ediacaran), petrographic features and recent U/Pb ages on single zircons (675 ± 13 Ma; Mayer, *in* Massironi et al., 2007), it can be correlated with the Cryogenian pluton of Igoudrane that crops out just northeast of the study area (Fig. 1; U/Pb on zircon 677 ± 19 Ma; Mayer, *in* Schiavo et al., 2007).

These plutons mainly consist of tonalites with traces of a low-grade metamorphism. As a whole they show a calc-alkaline low-K association (Fig. 3), i.e., abundant quartz, plagioclase frequently replaced by aggregates of epidote and sericite, K-feldspar, biotite replaced by chlorite, and clinopyroxene replaced by green hornblende.

Ediacaran volcanic suite

The Ediacaran volcanic and volcaniclastic suite does not display Pan-African folding and metamorphism and unconformably overlies the Cryogenian metasediments (Fig. 4A). The typical facies of this heterogeneous suite is related to volcanic activity between 570 and 545 Ma (U/Pb on zircon ages; Mifdal and Peucat, 1986; Cheilletz et al., 2002; Levresse et al., 2004; Massironi et al., 2007; Dal Piaz et al., 2007; Schiavo et al., 2007; El Boukhari et al., 2007) that was first defined in the region of Ouarzazate (Ouarzazate Group; Choubert, 1945, 1952; Hinderemeyer, 1953; Boyer et al., 1978). This volcanic sequence displays high-K calc-alkaline to shoshonitic compositions and includes intermediate to acid lavas, domes, ignimbritic flows, reworked tuffs, and volcanosedimentary deposits.

A rough subdivision of the Ouarzazate group limited to the Jebel Habab and Bou Zamour area is possible, distinguishing a basal sequence mainly composed of dacitic and andesitic flows (Jebel Habab dacitic-andesitic complex), and an upper sequence dominated by rhyolitic lavas and abundant ignimbrites (Takhatert complex; Hinderemeyer et al., 1977; Massironi et al., 2007).

The lower andesites are porphyric rocks with phenocrysts of plagioclase altered to albite, sericite and epidote assemblage, brown hornblende, chloritized biotite, and uralitized clinopyroxene. The groundmass is composed of altered plagioclase, quartz, chlorite, sericite, and abundant opaque minerals. The rhyolitic ignimbrites are, in contrast, composed of quartz and feldspar phenocrysts in a cryptocrystalline matrix. The volcanic and volcaniclastic series in the eastern margin of the study area may be subdivided into several volcanic complexes (Schiavo et al., 2007), characterized by rhyolitic lavas, domes, and ignimbrites and andesitic flows and dikes.

Ediacaran plutons

The Ediacaran plutons belong to two calc-alkaline suites characterized by low-K and high-K compositions (Fig. 3). The most important low-K granitoids are the Taouzzakt and Bou Teglimt plutons, both intruded into the Cryogenian metasediments and dated as early Ediacaran (572 ± 5 Ma U/Pb on zircon; De Wall et al., 2001; Cheilletz et al., 2002; Levresse et al., 2004; Schiavo et al., 2007). They are mainly composed of tonalites and quartz diorites with a primary mineral assemblage of quartz, plagioclase, K-feldspar, clinopyroxene, biotite, hornblende (pseudomorph on clinopyroxene), and a secondary assemblage of albite, chlorite, epidote, sericite, calcite, and actinolite (Fig. 2B). Among accessory phases, opaque minerals are abundant.

Diachronous bodies with similar high-K calc-alkaline compositions crop out in a wide sector of the study area. The major bodies are the Oussilkane (596 Ma ± 20 Ma U/Pb on zircon; Schiavo et al., 2007) and Bou Gafer plutons. The Oussilkane pluton is overlain by the Ediacaran volcanic suite and is in turn intruded by the two medium-sized Arharrhiz (571 ± 22.Ma U/Pb on zircon) and Igourdane bodies (Fig. 4B) (Errami et al., 1999; Schiavo et al., 2007; Dal Piaz et al., 2007). The Bou Gafer pluton intrudes the volcanic suite covering Oussilkane (Fig. 4C), but its stratigraphic relationship with both Arharrhiz and Igorudane is not yet constrained (Schiavo et al., 2007; Dal Piaz et al., 2007).

The Oussilkane pluton includes monzogabbros, monzonites, monzogranites, and syenite, representing a calc-alkaline high-K series that is more mafic with respect to the low-K granitoids (38.8% vs. 20% of mafic minerals), and is characterized by the presence of orthopyroxene (augite), clinopyroxenes (tremolite-actinolite series), biotite, and rare hornblende. In comparison with the low-K intrusives, these rocks are characterized by the relative abundance of K-feldspar with respect to plagioclase (17.8% in monzogabbro and/or monzodiorites, to 84% in syenite; Fig. 3) and by the presence of abundant pyroxenes (Fig. 2C).

The Bou Gafer granitoid has a less variable modal composition than the Oussilkane pluton. It mainly consists of a quartz monzonite with K-feldspar (often with widespread clay alteration), plagioclase, quartz, pyroxenes often completely altered by opaque minerals, and chloritized biotite. In the study area the Bou Gafer quartz monzonite can usually be distinguished by its abundance of ilmenite, magnetite, and hematite (Figs. 2D, 2E). The Aguensou subvolcanic granodiorite, which is overlain by the Ediacaran volcanic series, can be ascribed to the same igneous suite.

The differentiated products of the Arharrhiz and Igourdane granites can be distinguished from the other high-K granitoids by the albitic composition of the plagioclase and, particularly in the Arharrhiz granite, the lower abundance of mafic minerals (3%–4%), which for both plutons are mainly unaltered biotite and green hornblende (Fig. 2F).

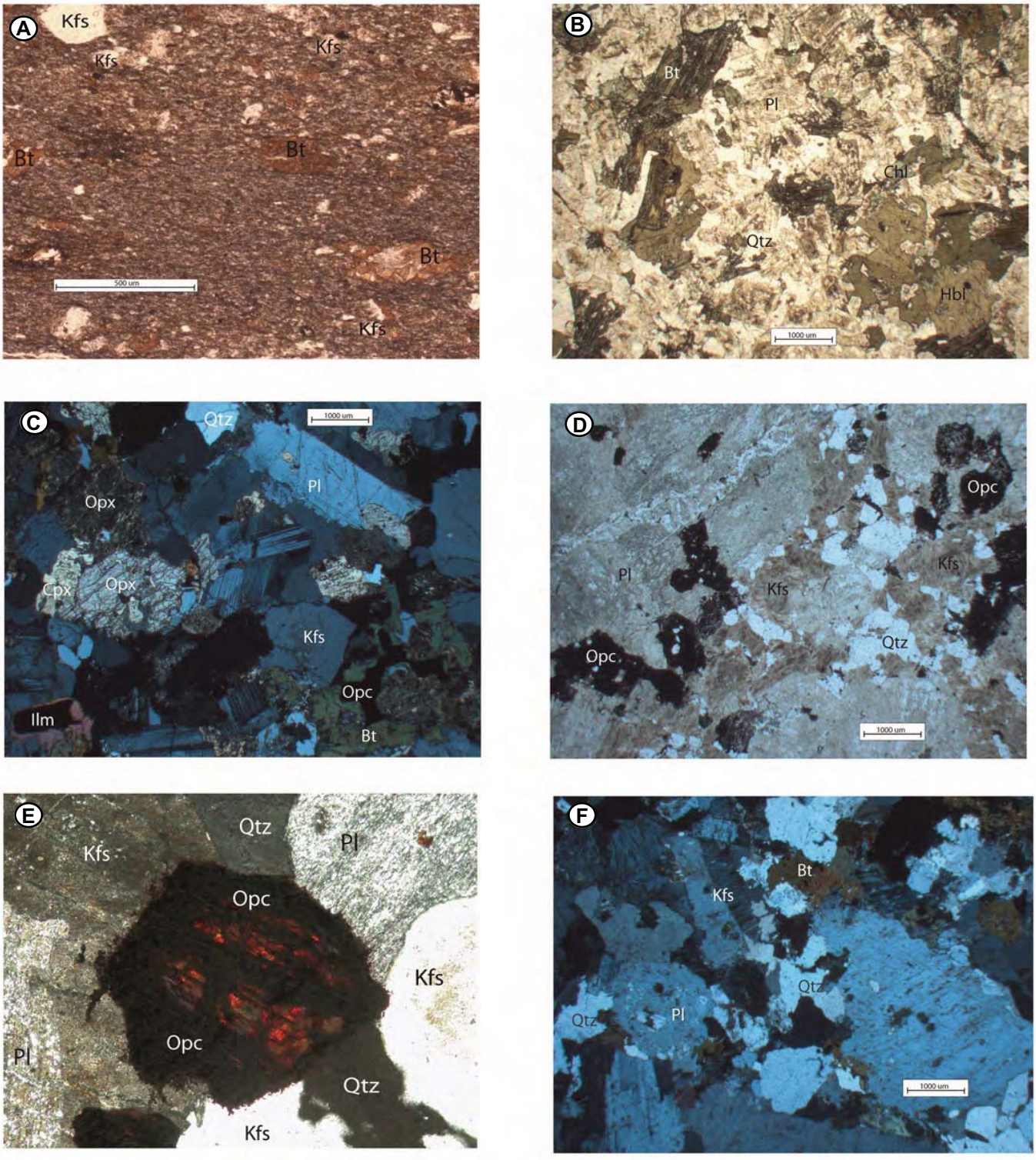

Figure 2. Thin sections. (A) Cryogenian metaturbidites: note abundant biotite. (B) Taouzzakt tonalite (low-K series). (C) Oussilkane monzonite (cross-polarized light). (D) Bou Gafer quartz monzonite: note pseudomorphs of opaque minerals on replaced pyroxenes. (E) Mafic crystal altered by opaque mineral. Opaque alteration minerals form dusty intergrowths in which reddish shades of hematite are evident (20× enlargement). (F) Arharrhiz granite (cross-polarized light). Kfs—K-feldspar; Bt—biotite; Pl—plagioclase; Chl—chlorite; Qtz—quartz; Hbl—hornblende; Opx—orthopyroxene; Ilm—ilmenite; Opc—opaque mineral.

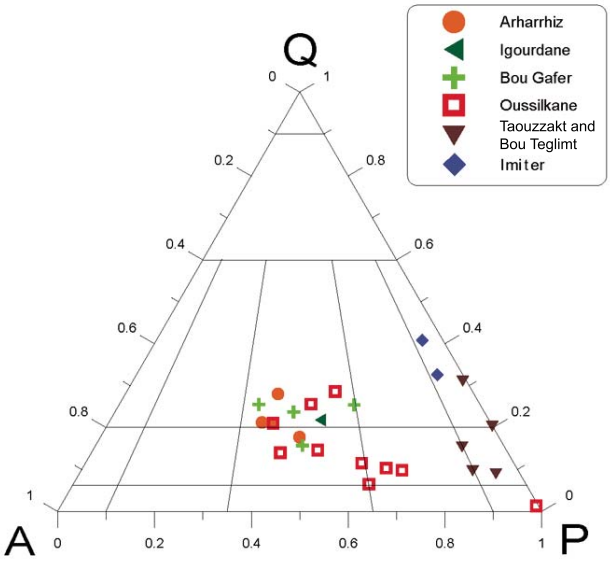

Figure 3. Modal analysis QAP (quartz–alkali feldspar–plagioclase feldspar) diagram of Cryogenian (Imider), Ediacaran low-K (Taouzzakt and Bou Teglimt) and high-K plutons (Oussilkane, Arharrhiz, Bou Gafer, Igourdane).

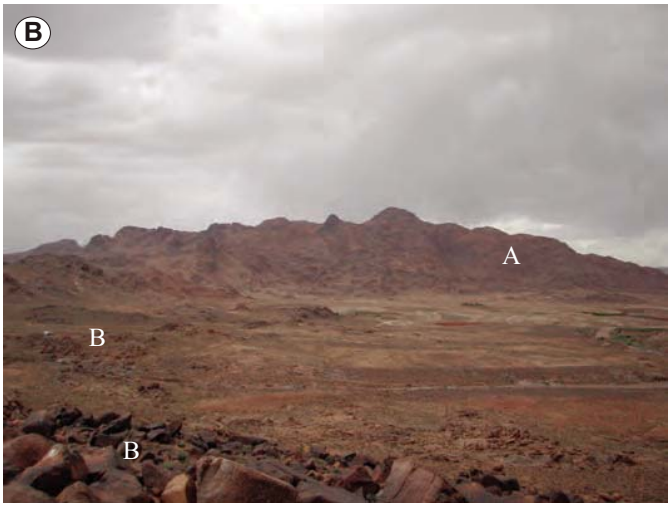

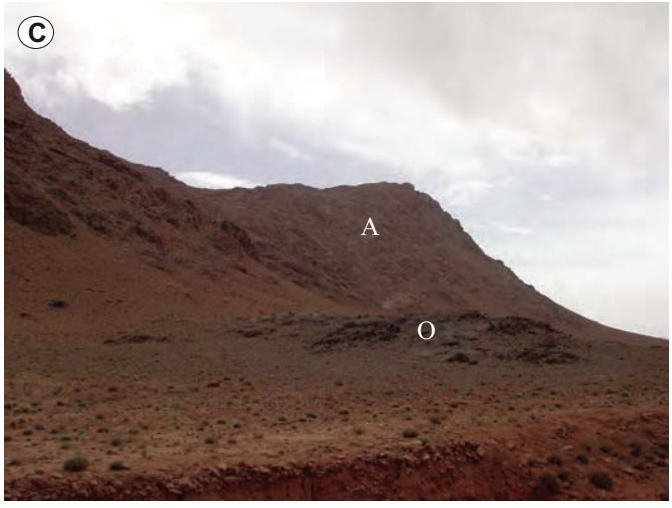

Figure 4. (A) Contact between Ediacaran upper volcaniclastic series (V) and Cryogenian metasediments (T) in Tirza-Ikkis area (see Fig. 10 for detailed location). (B) Ediacaran Arharrhiz granite (A); some outcrops of Bou Gafer quartz monzonite are also highlighted (B). (C) Intrusive contact between Arharrhiz granite (A) and Oussilkane monzonite (O; see Fig. 17 for detailed location).

Surface Alteration

Despite their composition, all the outcrops are more or less coated by an arid-environment alteration patina, the mineral composition of which is a mixture of Fe/Mn oxides and clay minerals, similar to many other desert varnish coatings (e.g., Hooke et al., 1969; Potter and Rossman, 1977, 1979; Dorn and Oberlander, 1981; Rivard et al., 1992). Scanning electron microscope images of varnished rock surfaces show a coating film as thick as 10 μm that consists of Si and Fe/Mn oxides arranged in laminae and is characterized by a sharp contact with the underlying fresh rock (Fig. 5). Over this coating clays and salts are scattered in microdepressions. The varnish coating, which can mask the spectral response of the rock's mineral assemblages (Fig. 5), strongly depends on weathering and erosion characteristics modulated by rock mineralogy and texture (Rivard et al., 1992). The foliated metaturbidites are generally covered by a surface regolith composed of varnished platy-like slabs, detached from the bedrock. The final effect is a non-uniform varnish coating. In contrast, the volcanic sequences are generally massive and more uniformly covered by the alteration patina. Granitoids are more likely to weather by granular disintegration, so that their varnish coating may be extremely variable and depends upon exposure to winds. Hence, desert varnish is widespread on the Oussilkane monzonite and less common on the more exposed rocks of the Arharrhiz and Taouzzakt bodies.

Faults and Veins

The study area is transected by a pervasive network of strike-slip and normal faults, often associated with veins and spatially related to dikes (Cheilletz et al., 2002; Massironi et al., 2007; Dal Piaz et al., 2007; Schiavo et al., 2007).

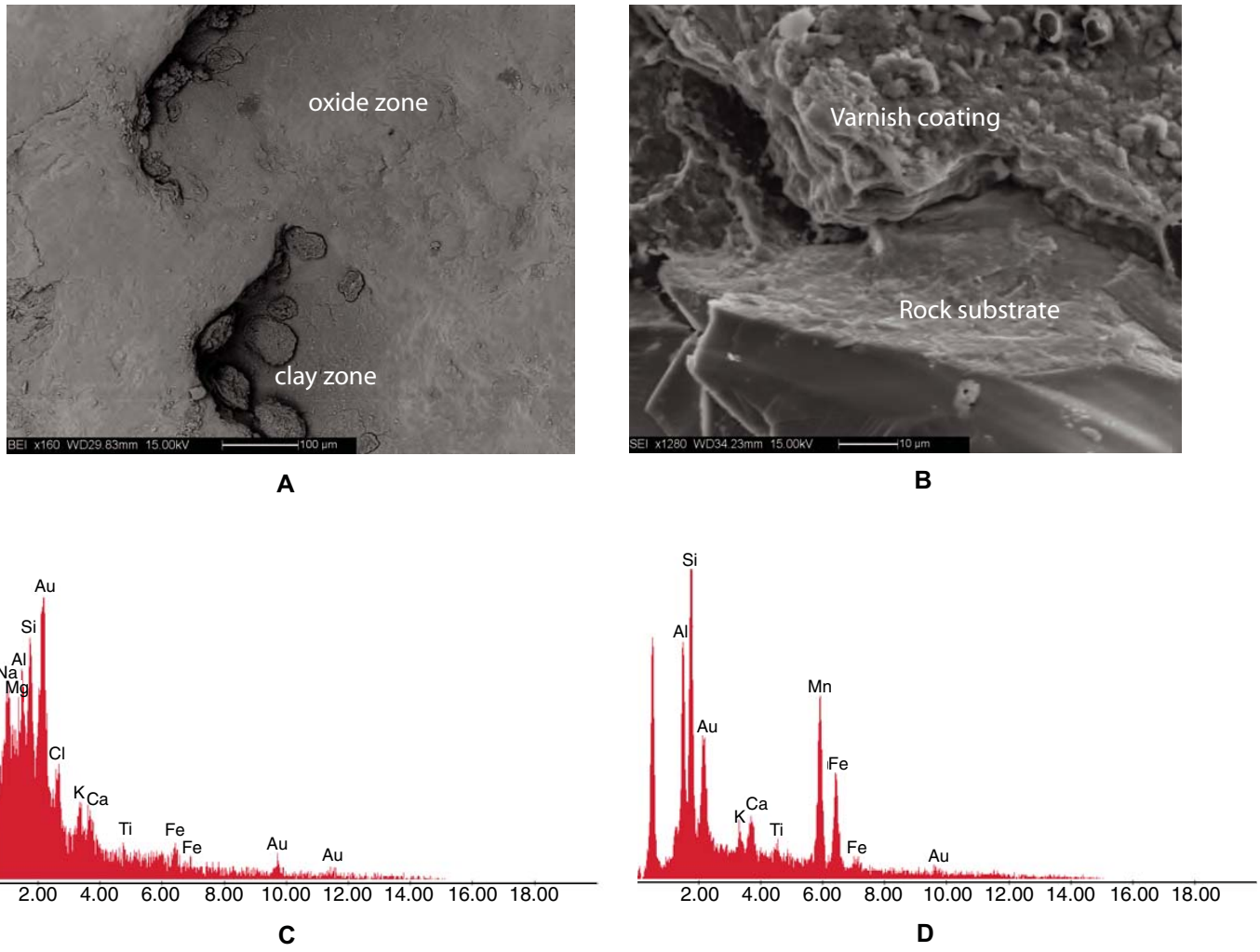

Figure 5. (A) Backscattered scanning electron microscope (SEM) image of varnished rock surface. Two alteration zones can be recognized: the real varnish coating and a superimposed discontinuous layer of clays and salts, generally concentrated in microdepressions. (B) Secondary electron SEM image of monzonite sample (Oussilkane pluton). The contact between the rock surface (quartz crystal) and the varnish is sharp. The varnishes are composed of irregular and often discontinuous layers or lenses 10 μm thick and oriented parallel to the rock surface. (C) Semiquantitative energy-dispersive spectrometry (EDS) spectra of clay zone show Na and Cl peaks that may be related to sodium chloride. Na, Ca, Mg, Fe, Al, and Si abundance are related to clay minerals. Au is derived from gold plating. (D) Semiquantitative EDS spectra of oxide zone showing peaks of Si, Mn, and Fe, the most abundant constituents of desert varnish. (Samples examined by SEM Camscan MX2500 operating at 20 kV and equipped with EDAX EDS for semiquantitative chemical analysis.)

Among the most important are (1) the east-west–trending fault system developed in the Imiter area and associated with a very important silver ore deposit (Cheilletz et al., 2002), and (2) the northwest-southeast Bou Zamour–Jebel Habab line, which is the tectonic boundary between the Cryogenian metasediments and a thick Ediacaran volcanic sequence filling an elongated half-graben structure (Fig. 1). In addition, minor northwest-southeast normal faults and a pervasive system of northeast to east-northeast dilational faults and veins developed in the study area (Fig. 6). Most of these faults were characterized by significant hydrothermal circulation, which occurred during and just after the volcanic activity in the Saghro area (Ighid et al., 1989; Ouguir et al., 1994; Cheilletz et al., 2002). Indeed, most of the northeast-southwest faults are associated with thick veins of hard quartz breccias with metallic mineralization and wide hydrothermal alteration halos in the hosting rocks. The mineralization is dominated by hematite found either as massive bodies associated with minor pyrite and chalcopyrite, or as a coating on fault surfaces (Figs. 7A, 7B). Kaolinite may locally occur at the mineralized vein borders. In the Imiter area the faults acted as preferred channels for deposition of the Ag-Hg sulfides of the large Imiter epithermal mine (Leistel and Qadrouci, 1991; Baroudi et al., 1999; Ouguir et al., 1994; Cheilletz et al., 2002; Levresse et al., 2004). In most cases the hardened fault breccias appear in relief with respect to softer and more eroded host rocks (Figs. 7C, 7D).

After the Pan-African activity, several faults and veins were reworked. In particular, during the Mesozoic continental rifting, some Jurassic dikes were intruded inside inherited deformation zones, whereas other faults, with evident strike-slip reactivation at the fault breccia boundaries, can be extended outside the Saghro Precambrian window, throughout the Paleozoic to Mesozoic sequences, suggesting some Alpine activity in the Atlas foreland (Massironi et al., 2007; Schiavo et al., 2007). Both Mesozoic and Alpine events have recently been proven by means of field analysis and fission track dating (Malusà et al., 2007).

REMOTE SENSING DETECTION OF THE MAJOR GEOLOGICAL UNITS AND MINERALIZED FAULT VEINS

The remote sensing analysis was carried out using ENVI software on ASTER 1B data acquired on 14 May 2001. The ASTER optics are composed of a nadir-pointing multispectral sensor and a backward-pointing sensor. The nadir-pointing sensor acquires 14 channels subdivided as follows: 3 VNIR (15 m/pixel), 6 SWIR (30 m/pixel), 5 TIR (90 m/pixel; Yamaguchi et al., 1998; Abrams 2000; Table 1). The backward-pointing channel is centered in the near infrared corresponding to channel 3 of the nadir-pointing sensor (Yamaguchi et al., 1998).

The SWIR bands were first corrected for cross-talking effects in accordance with Hewson et al. (2005). The 14 bands were resampled at 15 m/pixel, coregistered, and orthorectified using the ASTER-derived digital elevation model (DEM). During the orthorectification process, nearest-neighbor resampling was preferred to bilinear and cubic convolutions in order to better preserve the spectral information of the images. VNIR and SWIR ASTER data were converted into ground reflectance by correcting for the atmospheric effects. This was performed using the second simulation of a satellite signal in the solar spectrum (6S) code (Vermote et al., 1997). The 6S code was applied with standard atmospheric profiles, the desert aerosol model, and 100 km of visibility range, the latter selected in view of the very clear atmospheric conditions usually occurring in the area when no desert storms or clouds are present.

VNIR/SWIR False Color Composites

Geological interpretation of remotely sensed data is very effective when the ASTER 7-3-1 RGB (red-green-blue) false color composite is used. The choice of band 7 was made in order to highlight both the Al-OH absorption of white mica and clays and the Mg-OH absorptions of phyllosilicates, amphiboles, and epidote (Fig. 8). In fact, in the study area band 7 is highly correlated with both band 8 and band 6, in which Mg-OH and AL-OH absorptions are respectively centered (Table 2a). Band 1 is representative of charge transfer of Fe ions in phyllosilicates, amphiboles, pyroxenes, and ferric oxides (hematite and goethite) (Fig. 8). Fe crystal field absorption and high reflectance by vegetation cover are recorded by band 3. The 731 false color image clearly highlights the boundaries among Cryogenian turbiditic metasediments, Ediacaran andesites, and rhyodacitic sequences, and major intrusives are clearly distinguishable

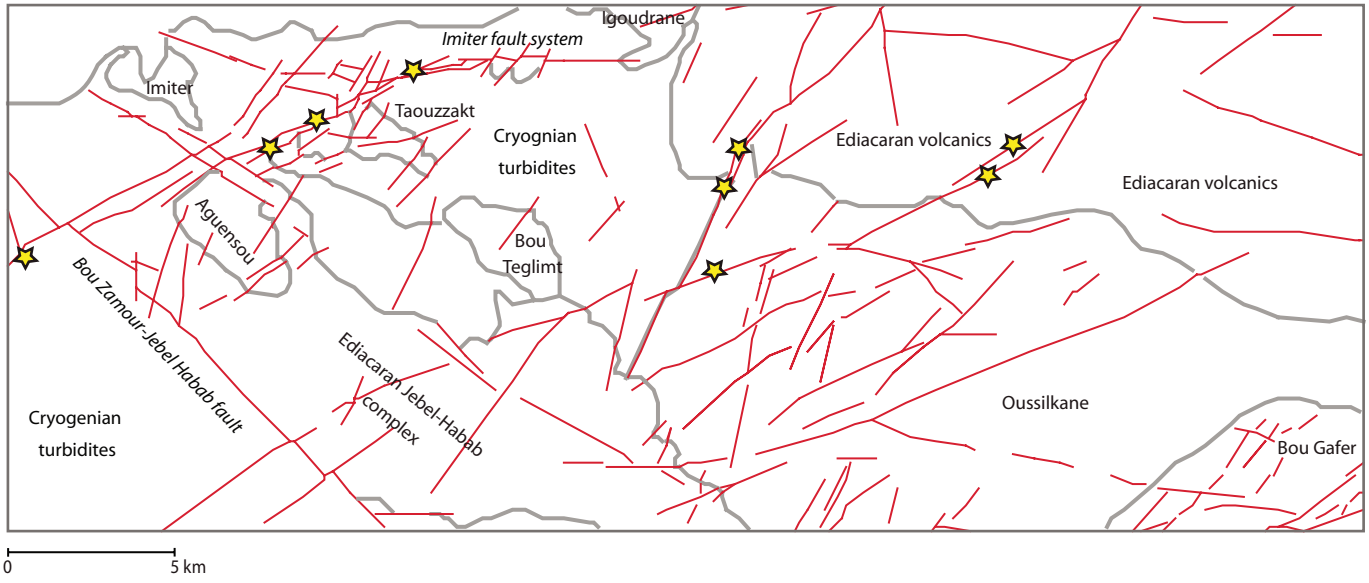

Figure 6. Geological sketch of the study area in which faults have been highlighted; stars indicate mineralized fault breccias (location in Fig. 1).

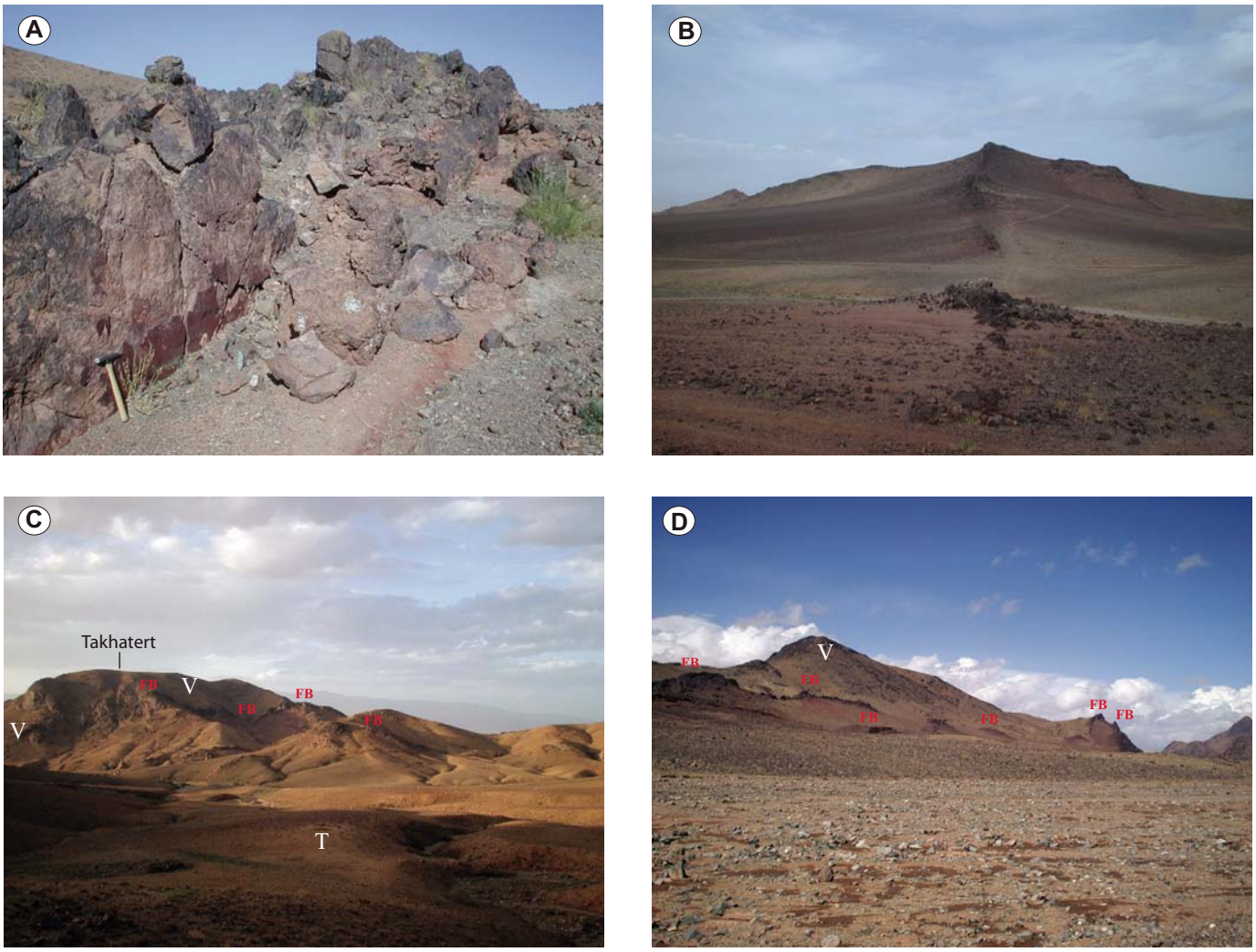

Figure 7. (A) Fault rocks in the Tirza-Ikkis area are characterized by mineralized (mainly hematite) quartz fault breccias often bounded by sharp planes coated by hematite. (B) Massive hematite vein cutting Ediacaran volcanic series and the early Cryogenian metasediments of the Boumalne "boutonniere." (C) The Tissidelt-Takhatert rhyolitic dome of the Ediacaran volcaniclastic series (V) is cut by mineralized faults (fault breccias, FB) in relief and overlies early Cryogenian metasediments (see Fig. 9 for detailed location). (D) Ediacaran volcaniclastic series cut by mineralized faults in relief (FB) in the Tirza-Ikkis area (see Fig. 10 for detailed location).

(Figs. 9 and 10). The turbidites, generally dominated by phyllosilicates, appear blue because they are characterized by a moderate reflectance in the visible wavelength and a relatively low reflectance in infrared wavelengths, particularly in relation to the OH absorption bands of biotite and chlorite (Mg-OH), and sericite (Al-OH). The volcanic suites show a high variability with dominant dark blue to magenta colors. The dark blue probably reflects the presence of andesites, which are characterized by hornblende, chloritized biotite, and abundant saussirite (sericite and epidote) in the matrix derived from alteration of plagioclase. Both the Al-OH and Mg-OH absorptions of these minerals lower the reflectance of ASTER bands in the short wavelength infrared. The magenta to reddish colors are due to a variable content of chlorite in the rock or, more likely, of clays and nannocrystalline ferric oxides in the widespread alteration patina. The plutons have a variety of reddish colors, reflecting a higher reflectance in band 7 than in bands 3 and 1. In addition, different reddish colors among plutons may also be related to actual variations in the content of mafic minerals and altered feldspars and/or variable desert varnish coating.

VNIR/SWIR Band Ratios

As noted from the ASTER 7-3-1 false color composite, the major geological boundaries between turbidites, volcanic sequences, and the main intrusives are visible and well defined, as well as those of some minor intrusive bodies, but many more features can be extracted using band ratios focused on specific absorptions. In this work RGB false color composites of ASTER ratios 4/6–2/1–4/3 and 4/8–2/1–4/3 were used (Figs. 9 and 10). The 4/8 ratio is important for highlighting the Mg-OH bond stretching of biotite, chlorite, epidote, and amphiboles (Fig. 8) that can be present inside Cryogenian turbidites and in variable percentages in volcanic and plutonic rocks. The 4/6 ratio was selected for detecting the Al-OH absorption of kaolinite and other clay minerals, which are alteration products of K-feldspar, and of sericite, typical of the saussuritic alteration of plagioclase. The 2/1 and 4/3 ratios were selected for the absorption bands due to Fe charge transfer and crystal field effects, respectively. In addition, the 2/1 ratio

TABLE 1. ASTER DATA BAND RANGES AND SPATIAL RESOLUTION

Subsystem	Band	Spectral range (μm)	Spatial resolution (m)
VNIR	1	0.52–0.60	15
	2	0.63–0.69	
	3	0.76–0.86	
SWIR	4	1.60–1.70	30
	5	2.145–2.185	
	6	2.185–2.225	
	7	2.235–2.285	
	8	2.295–2.365	
	9	2.36–2.43	
TIR	10	8.125–8.475	90
	11	8.475–8.825	
	12	8.925–9.275	
	13	10.25–10.95	
	14	10.95–11.65	

Note: References: Yamaguchi et al. (1998); Abrams (2000). ASTER—Advanced Spaceborne Thermal Emission and Reflection Radiometer; VNIR—visible and near infrared; SWIR—shortwave infrared; TIR—thermal infrared.

can emphasize the S valence to conduction band gap of sulfurs. The final results of the use of these band ratios is that fault breccias, enriched in Fe oxides and associated with widespread hydrothermal alteration, were highlighted, and some barely visible boundaries between different volcanic sequences and between minor intrusives and volcanic rocks were detected (Figs. 9 and 10).

In the ASTER 4/8–2/1–4/3 color composite (Figs. 9C and 10C), the metaturbidites appear dark due to the abundance of biotite, with a light reddish color along pelitic layers probably due to enhanced absorption in band 8 of chlorite, epidote, and actinolite in fine-grained rocks. In addition, scattered green patches are probably related to hematite in the inhomogeneous desert varnish (regolith of varnished plate-like slabs). The volcanic sequences show green to cyan colors, primarily reflecting the strong and widespread desert varnish coating and secondarily the variable content of Fe present in hornblende, epidote, and opaque minerals. The plutons generally show a reddish magenta color that simultaneously reflects the Mg-OH absorptions of phyllosilicates, epidote, amphiboles, and the influence of Fe absorptions of the same mafic minerals or of their hematitic alteration (e.g., Aguensou Habab, Imider, Bou-Teglimt, and Oussilkane). The plutons locally show cyan-dominated patches, reflecting the dominant presence of hematite as an alteration of mafic minerals and/or in the desert varnish.

The false color composite 4/6–2/1–4/3 is best suited for the detection of hydrothermal alteration around mineralized veins. The veins display a typical cyan tonality in both the composite ratios, due to ferric oxides and sulfurs, but in the 4/6–2/1–4/3 they are also associated with whitish to pale yellow colors where kaolinitization induced by hydrothermal alteration is more developed (Fig. 9D). Because turbidites have colors similar to those displayed in the 4/8–2/1–4/3 image, the Al-OH absorption of sericite is comparable to that of the Mg-OH absorption of biotite, chlorite, and epidote. The same color of 4/8–2/1–4/3 is also displayed by the volcanic sequences, proving the strong contribution of desert varnish to the VNIR/SWIR reflectance of these rocks. In contrast, the plutonic rocks appear different in 4/6–2/1–4/3, with only a slight magenta tone superimposed on a dominant blue to cyan color (Figs. 9D and 10D). This characteristic color reflects a weak contribution of Al-OH absorption. This is not surprising because the granitoids that crop out in the study area are characterized by a virtual absence of white mica (see the Geological Framework), so that most of the Al-OH absorptions are related only to the kaolinite and/or saussirite derived by alteration of K-feldspars and plagioclase, respectively. This

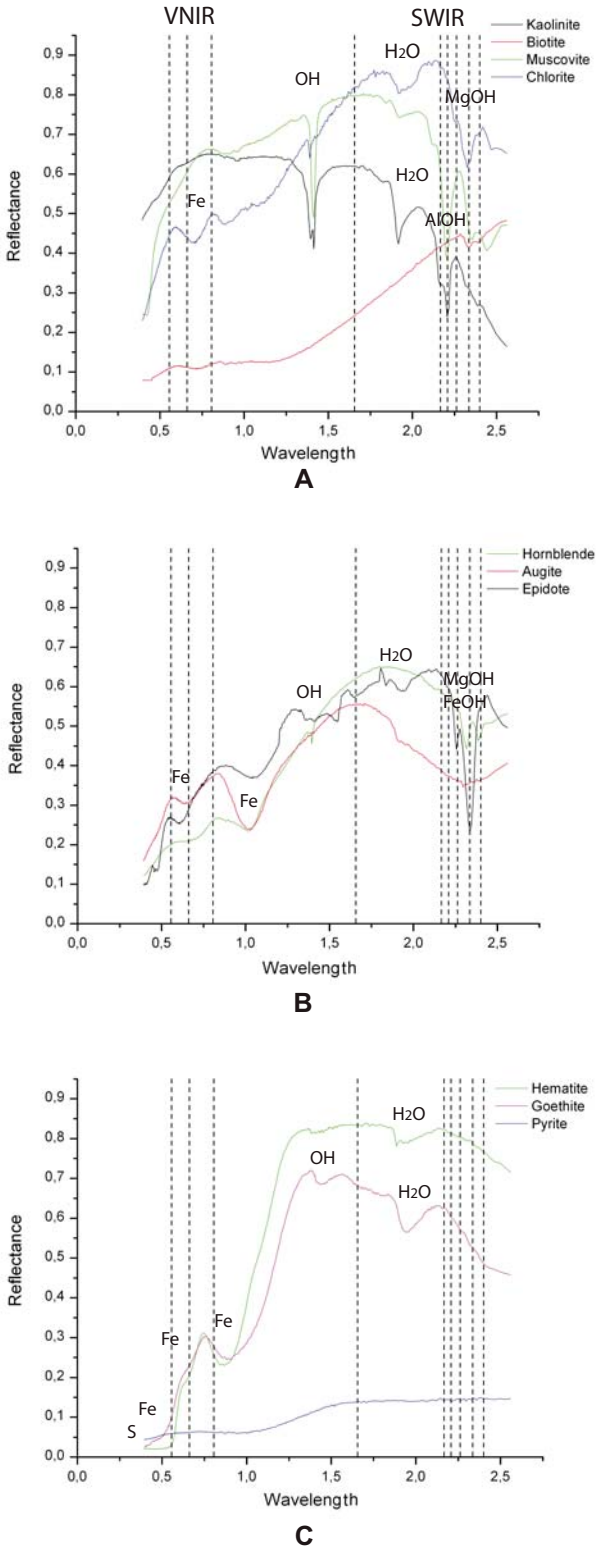

Figure 8. VNIR/SWIR (visible and near infrared, shortwave infrared) signatures of selected minerals versus ASTER (Advanced Spaceborne Thermal Emission and Reflection Radiometer) VNIR and SWIR central bands. (A) Chlorite, biotite, muscovite, kaolinite. (B) Hornblende, augite, epidote. (C) Goethite, hematite, pyrite (from Clark et al., 1990).

TABLE 2A. CORRELATION MATRIX OF THE ASTER DATA IN THE STUDY AREA

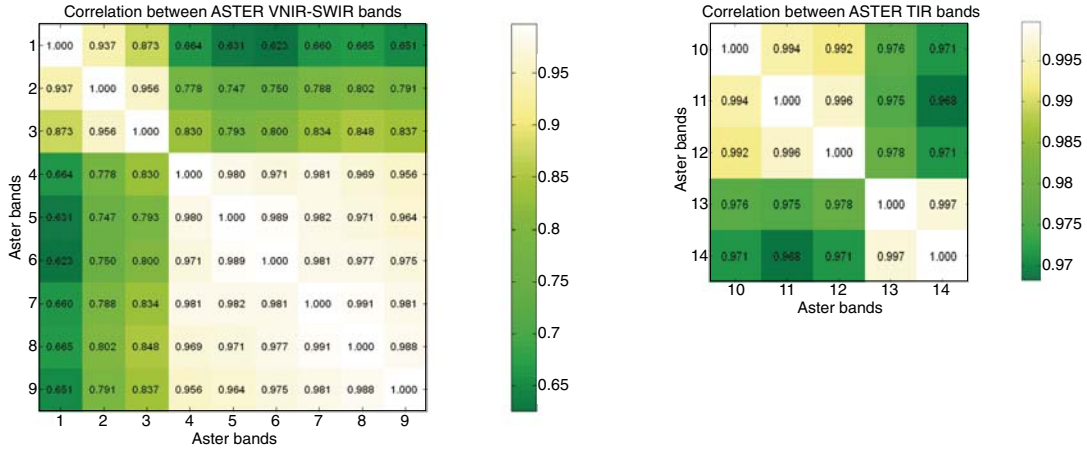

TABLE 2B. CORRELATION MATRIX AND EIGENVECTORS OF THE PRINCIPAL COMPONENTS ANALYSIS CALCULATED FOR THE FIRST NINE BANDS OF THE ENTIRE ASTER SCENE

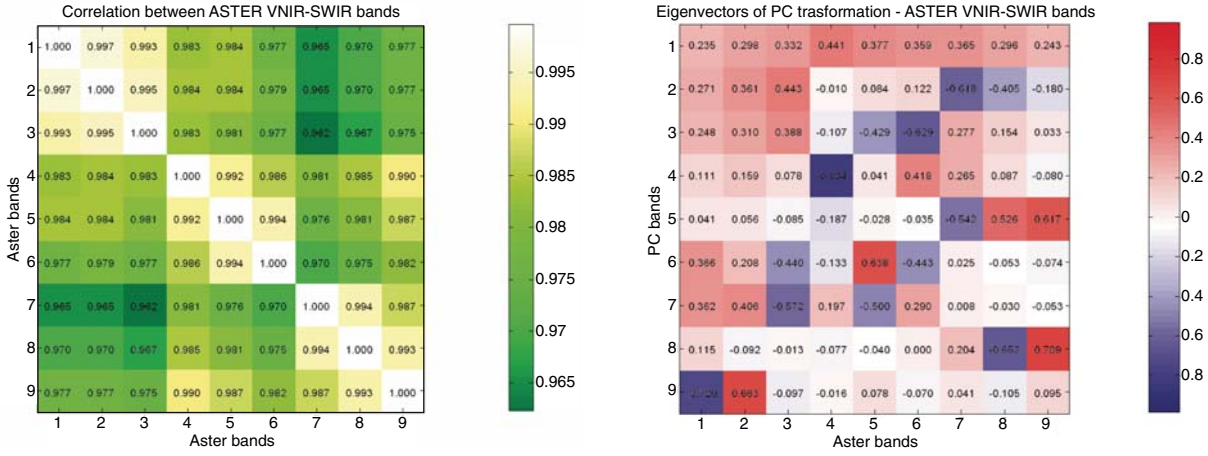

hypothesis is further constrained by the relative band-depth image (RBD) for Al-OH absorption. The RBD elaboration is a ratio where the numerator is the sum of bands representing the shoulder of an absorption feature (in this case bands 5 and 7) and the denominator is the band nearest to the absorption peak (in this case band 6) (e.g., Crowley et al., 1989; Rowan and Mars, 2003). The result shows the highest concentration of Al-OH absorptions for high-K intrusions and, in particular, for the Oussilkane and Bou Gafer plutons, where feldspars are particularly altered (Fig. 11).

Principal Components Analysis

Principal components analysis (PC) has been applied to the whole scene, and the PC9, PC7, and PC2 bands were helpful for detecting veins and alteration halos associated with faults. In Table 2b the correlation matrix and PC eigenvectors are presented. PC9 is principally positively loaded by band 2 (+0.66) and negatively by band 1 (–0.72), and reflects the presence of hematite and sulfurs in fault breccias (pale gray to white in the image). In contrast, PC7 has a medium negative eigenvector for band 3 (–0.57), which is affected by the Fe crystal field effect, but has a medium positive one for band 1 (0.36), which reflects the stronger Fe charge transfer absorptions effects; consequently, mineralized veins are generally dark gray in the related image. PC2 is characterized by strong negative loading by band 7 (–0.62), which is located in a relative peak between OH absorptions, and medium positive loading by bands 2 and 3 (0.36 and 0.44, respectively); therefore veins are dark gray in the related image if mineralized and pale gray if associated with hydrothermal alteration and clay minerals. In the RGB composites of PC9-PC7-PC2, the mineralized veins are therefore outlined by a red to magenta color corresponding to the variable content of kaolinite and hematite (Fig. 12).

REMOTE SENSING DETECTION OF THE EDIACARAN PLUTONS

The Cryogenian and low-K Ediacaran granitoids that crop out in the Saghro massif are always bounded by volcanic and metaturbiditic rocks, so that their boundaries are clearly distinguishable using the procedures described in the previous section. In contrast, the high-K Ediacaran plutons (Oussilkane, Bou Gafer, Arharrhiz and Igorudane) are directly in contact with each other, hence specific image processing steps are needed. As can be clearly seen from the QAP (quartz–alkali feldspar–plagioclase feldspar) diagram of Figure 3, these plutons are very similar in composition, most of them having similar proportions of mafic minerals. Nonetheless, as already noted, they can differ in the mafic

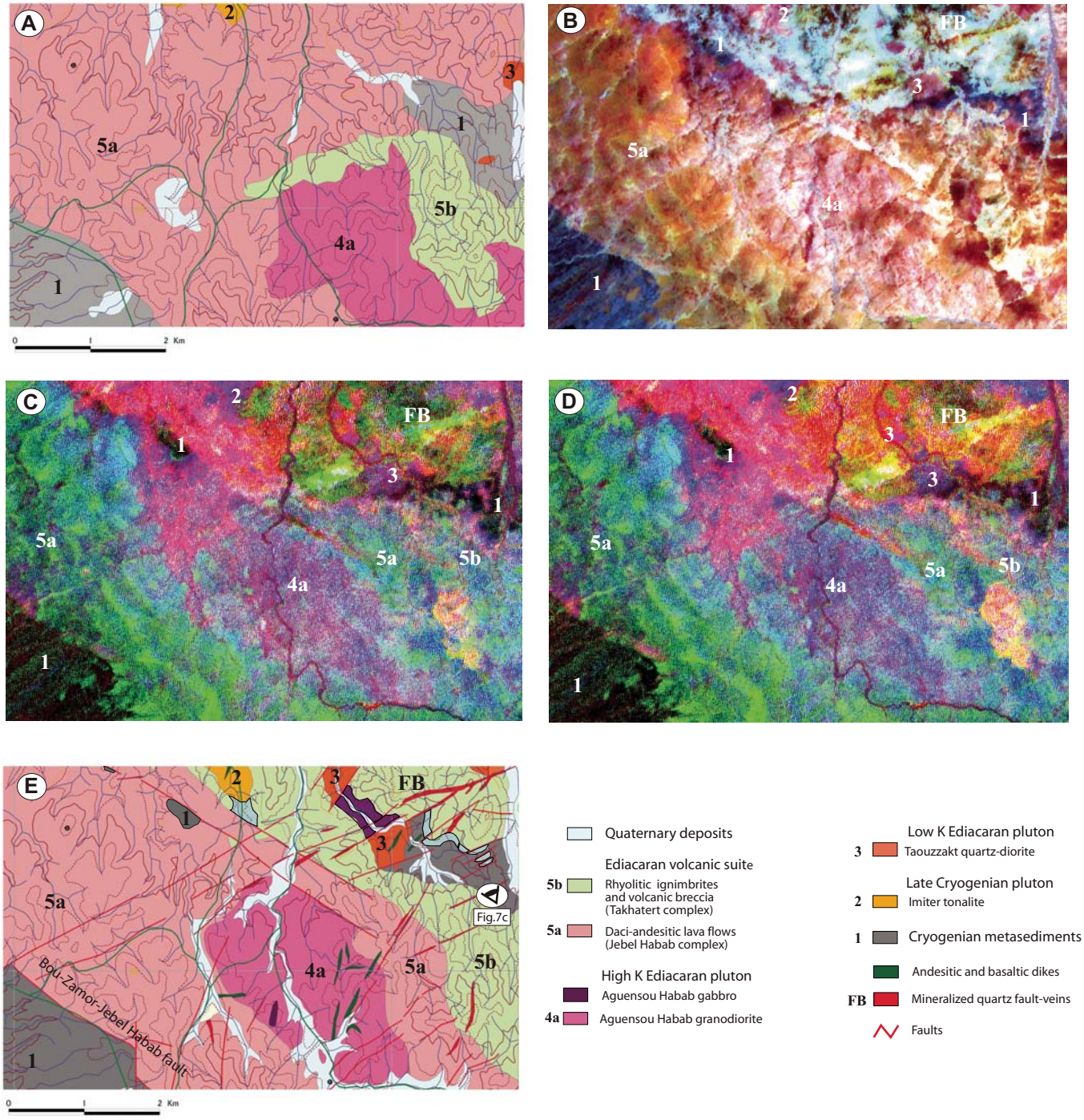

Figure 9. Remote sensing interpretation of the Tissidelt Takhatert–Bou Zamour area (location in Fig. 1). (A) Excerpt from the 1:200,000 geological map (redrawn after Hinderemeyer et al., 1977). (B) Saturation stretch of ASTER (Advanced Spaceborne Thermal Emission and Reflection Radiometer) 7-3-1 RGB (red-green-blue) false color composite. Cryogenian metaturbidites (1) boundaries are clearly visible; Imider tonalite (2) and Ediacaran low-K (3) granitoids are recognizable from surrounding rocks; mineralized faults (fault breccias, FB) are recognizable; boundaries between the Aguensou Habab high-K pluton (4a) with respect to the Ediacaran upper volcaniclastic series (5a) are unclear. (C) ASTER RGB ratio image 4/8–2/1–4/3; all objects delimited in ASTER false color composites are clearly detectable. In addition, the Aguensou Habab pluton is extremely well delimited by higher Mg-OH absorption, whereas the Ediacaran volcaniclastic series are dominated by the oxides of the alteration patina (green and cyan colors). (D) ASTER RGB ratio image 4/6–2/1–4/3: the mineralized fault-breccia (cyan) and the related alteration halos (yellow) are particularly evident, whereas the Al-OH absorptions associated with plutons are weak. (E) Final geological map resulting from remote sensing interpretation and field checks (some lithological units are too small to be distinguished only using remote sensing).

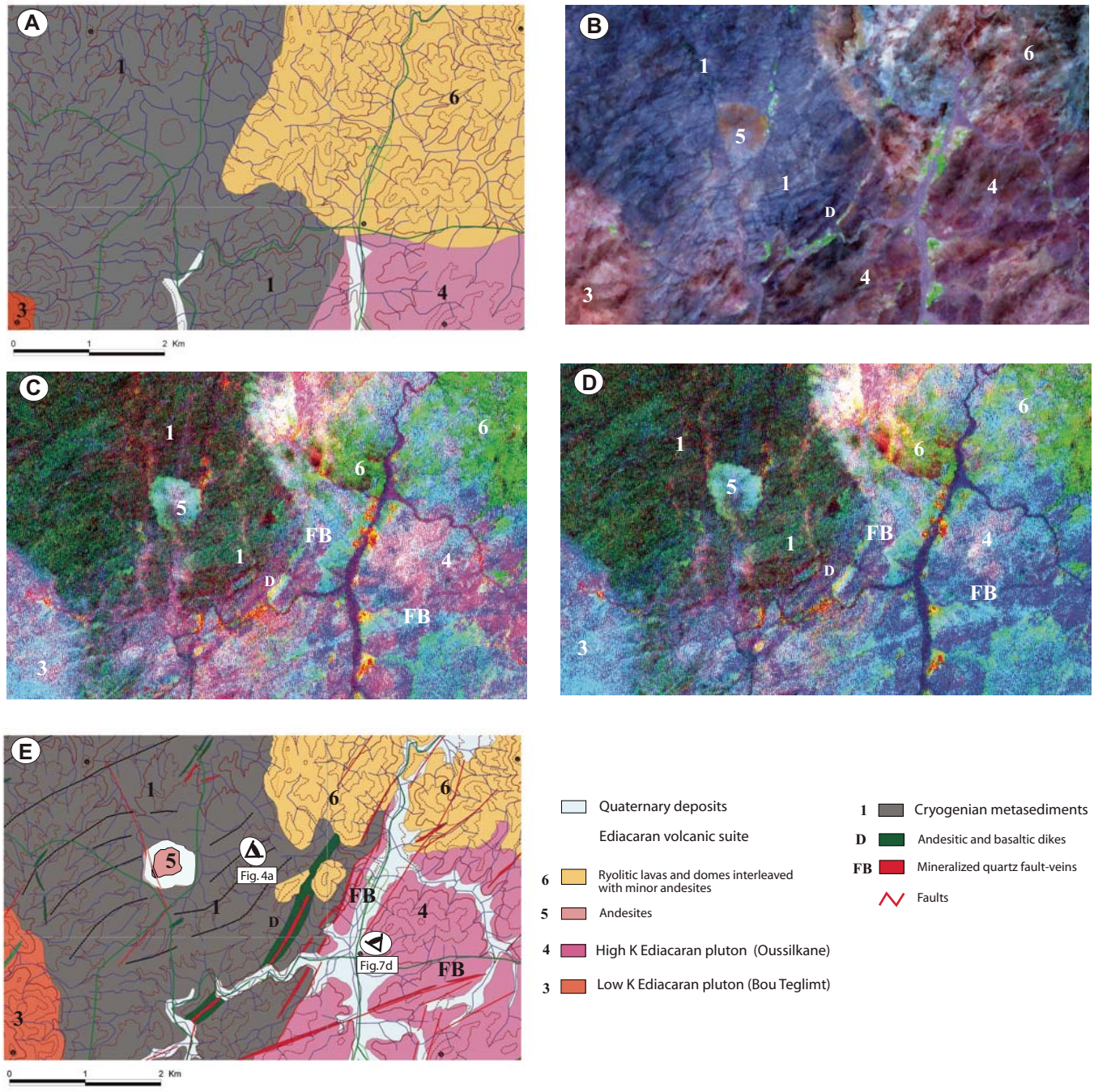

Figure 10. Remote sensing interpretation of the Tirza-Ikkis area (location in Fig. 1). (A) Excerpt from the 1:200,000 geological map (redrawn after Hinderemeyer et al., 1977). (B) ASTER (Advanced Spaceborne Thermal Emission and Reflection Radiometer) 7-3-1 RGB (red-green-blue) false color composites: boundaries between Cryogenian metasediments (1), Ediacaran Bou Teglimt tonalite (3), Upper Neoproterozoic volcaniclastic series (5, 6), and Oussilkane monzonites (4) are clearly visible and better delineated with respect to the existing geological map; in addition andesitic and basaltic dikes in metaturbidites are well highlighted (D). (C) ASTER RGB ratio-image 4/8–2/1–4/3; all objects delimited in the ASTER false color composites are clearly detectable; the only exception is andesitic dikes in metaturbidites. In addition, Late Neoproterozoic volcanic sequences (6) are easily recognized, assuming mainly greenish colors; intrusives (3, 4) and mineralized fault breccias (FB) become evident with blue to magenta and cyan colors, respectively. (D) ASTER RGB ratio-image 4/6–2/1–4/3 showing an Al-OH absorption of the Oussilkane monzonite slightly higher than the confining units. (E) Final geological map resulting from remote sensing interpretation and field checks.

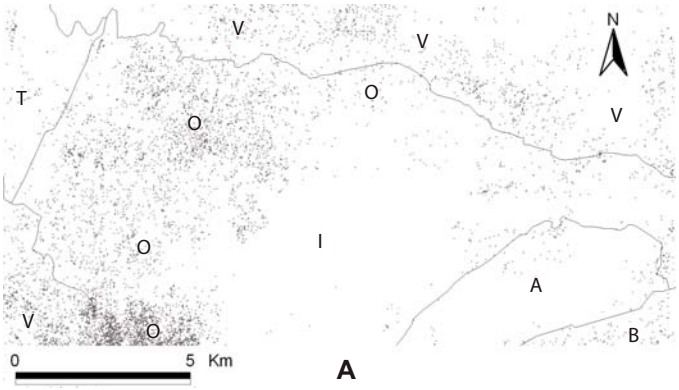

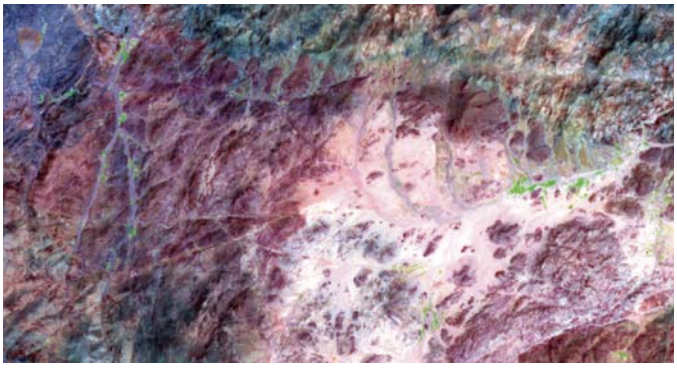

Figure 11. (A) Relative band-depth (RBD) image for Al-OH absorption (6) showing the highest concentration of Al-OH absorptions for Oussilkane and Bou Gafer plutons. (B) RGB (red-green-blue) 731 false color composite of the same area as A.

phases, the degree of hydrothermal alteration, and the surface alteration patina. The following paragraphs describe the image processing and results obtained using the TIR and VNIR/SWIR ASTER bands with the specific aim of mapping high-K Ediacaran plutons.

TIR Data Analysis

Despite their low resolution (90 m), the thermal infrared data are generally considered the most appropriate for identifying granitoid rocks (e.g., Sabins, 1996; Drury, 1997; Hook et al., 1999) because TIR spectra are only weakly disturbed by the desert varnish, which can have a detectable influence only if dominated by clay minerals (Salisbury and D'Aria, 1992; Christensen and Harrison, 1993). Spectra of granitoid rocks and silicates characteristically show a broad emission minimum (Reststrahlen band) in the 8.5–14 µm interval (Si-O stretching region), and a well-defined maximum (Christiansen frequency peak) in the 7–9 µm interval. The position and depths of both the Reststrahlen and Christiansen features vary according to the quartz content. In particular, the location of both the Christiansen maximum and the Reststrahlen minimum migrate to longer wavelengths as mineral and rocks become more mafic (Hunt, 1980; Salisbury and D'Aria, 1992; Sabine et al., 1994; Hook et al., 1999). As expected, the spectral signatures derived from the ASTER thermal bands, on sites of well-constrained lithological attribution, show similar trends for all the high-K plutons and generally higher emission by the more mafic ones (Oussilkane and Bou Gafer) (Fig. 13A). The Arharrhiz granite is characterized by a higher slope between band 13 and the other bands, where the Reststrahlen minimum is likely to be located. In contrast, the mafic Oussilkane pluton shows higher emissions at lower wavelengths (bands 10, 11, 12), probably influenced by the Christiansen maximum and the shifting toward longer wavelengths of the Reststrahlen minimum (Fig. 13A). So the 14–13–10 false color composite was chosen, and since all ASTER thermal bands are highly correlated (Table 2a), a decorrelation stretch was applied. The result clearly highlights the Arharrhiz granite in orange-yellowish colors (emission minima involving band 10) and the Oussilkane monzonite in a blue color (higher emission in band 10 in comparison with the other plutons). The Bou Gafer and Igourdane bodies are not well defined, though the common orange tonality of these plutons may indicate their intermediate composition, between the Arharrhiz granite and the Oussilkane monzonites (Fig. 13B).

Thermal band ratios were selected through a quantitative analysis of the spectral signatures directly derived from the ASTER image on sites of known lithology. The analysis was achieved in the following steps (Table 3a).

1. All the absolute differences between bands were calculated for each granitoid.

2. For each difference of step 1, the absolute differences between granitoids were calculated. Steps 1 and 2 can be summarized with the following simple formula:

$$\left\| b_{xg1} - b_{yg1} \right| - \left| b_{xg2} - b_{yg2} \right\| \quad , \qquad (1)$$

where b_{xgn} and b_{ygn} are reflectance values of a given couple of bands related to the specific granitoid *gn*.

3. For each pluton, all the minimum values among the differences obtained in step 2 were selected; these values indicate the potential for each band couple to discriminate a specific pluton, the highest minimum differences indicating the best band ratios for this purpose.

4. To avoid conflicts between ratios, which may be suitable for more than one pluton, the three highest values were considered for the final band ratio selection.

According to this procedure, the best band ratio for the Oussilkane monzonite is 14/12 (Table 3a; Fig. 13C), for the Arharrhiz and Bou Gafer plutons it is 14/10 (Table 3a; Fig. 13D), and for the Igourdane it is 13/14 (Table 3a; Fig. 13E). Therefore, the 14/12–14/10–13/14 set was selected and enhanced using a decorrelation stretch (Fig. 13F). In this false color image the Oussilkane monzonite (red to magenta colors in Fig. 13F) is clearly separated from the Igourdane and Arharrhiz granites (green to cyan colors in Fig. 13F), and the Bou Gafer has much more variable tonalities due to its intermediate composition.

VNIR/SWIR Data Analysis

FieldSpec®- and ASTER-derived rock signatures of granitoids

Most of the processing of VNIR/SWIR data for the high-K pluton detection was qualitatively supported by spectroradiometric analyses carried out on rock samples or on the ASTER image. Spectral signatures of samples representative of the high-K plutons of Oussilkane, Bou Gafer, and Arharrhiz were measured with the Analytical Spectral Device Inc. FieldSpec®

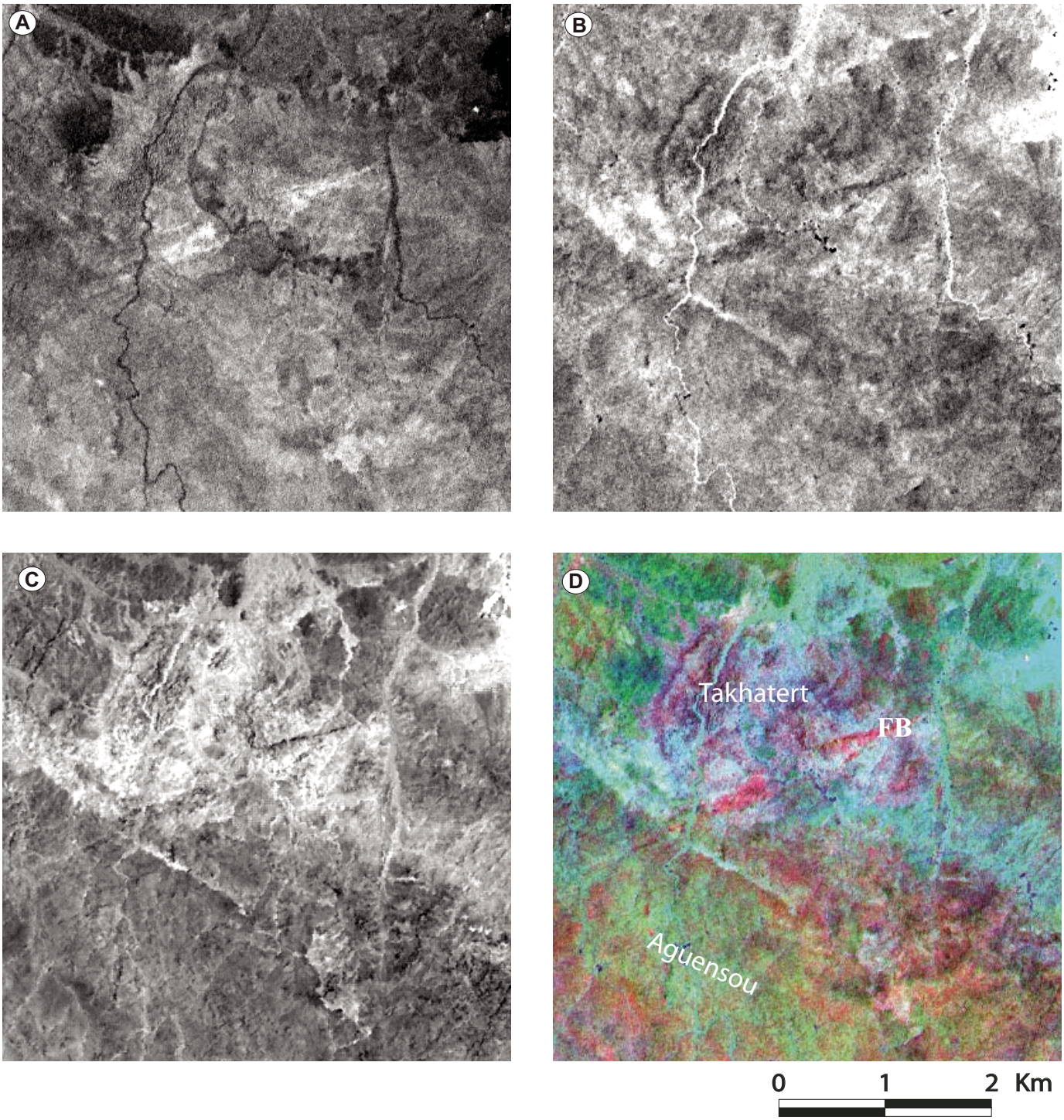

Figure 12. ASTER (Advanced Spaceborne Thermal Emission and Reflection Radiometer) principal components (PC) analysis for mineralized fault vein detection in the Tissidelt Takhatert area (location in Fig. 1). (A) PC9. (B) PC7. (C) PC2. (D) PC9-PC7-PC2 RGB (red-green-blue) false color composite. Fault mineralized breccias (FB) and related alteration halos are red to magenta depending on the variable content of kaolinite and hematite; the Takhatert rhyolitic dome and ignimbrites show dark magenta colors since they are characterized by intense hydrothermal alteration.

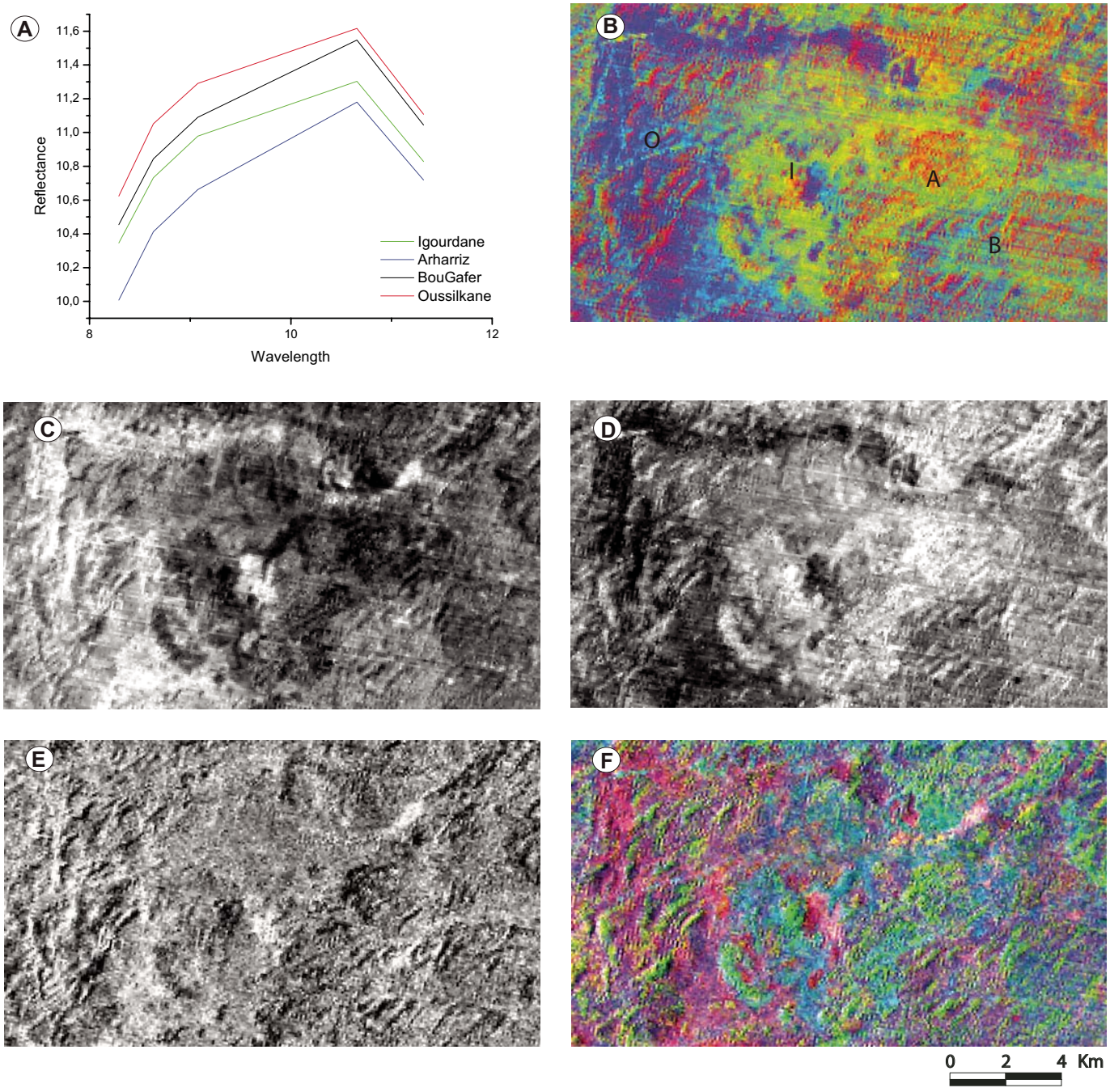

Figure 13. (A) TIR (thermal infrared) ASTER (Advanced Spaceborne Thermal Emission and Reflection Radiometer) signatures from ROI (regions of interest) centered at sampling position of Oussilkane, Bou Gafer, Igourdane, and Arharrhiz bodies (the ROI from which the signatures were derived are highlighted in Fig. 17B). (B) Decorrelation stretch of RGB (red-green-blue) ASTER 14–13–10 false color composite. The more mafic Oussilkane pluton (O) has blue colors, the more sialic Arharrhiz (A) granite is dominated by red; Bou Gafer (B) and Igourdane (I) have more variable and intermediate colors. (C) Band ratio 12/14, in which the Oussilkane monzonite shows the highest gray values. (D) Band ratio 14/10, in which the Arharrhiz pluton shows the highest gray values followed by the Bou Gafer quartz monzonite. (E) Band ratio 13/14, in which Igourdane and Bou Gafer plutons show higher gray values. (F) Decorrelation stretch of RGB 12/14–14/10–13/14 in which the Oussilkane monzonites are clearly distinguishable from the Arharrhiz and Igourdane granites, whereas the Bou Gafer quartz monzonite is characterized by variable tonalities.

TABLE 3A. SELECTION OF BAND COUPLES BEST SUITED FOR DISCRIMINATING THE EDIACARA PLUTONS ON TIR

BAND COUPLE	Absolute difference between Oussilkane Bou Gafer	Absolute difference between Oussilkane Arharrhiz	Absolute difference between Oussilkane Igourdane	Minimum absolute difference for Oussilkane	Absolute difference between Bou Gafer Arharrhiz	Absolute difference between Bou Gafer Igourdane	Absolute difference between Bou Gafer Oussilkane	Minimum absolute difference for Bou Gafer
10-11	0.037631	0.022705	0.041558	0.022705	0.014926	0.003927	0.037631	0.003927
10-12	0.030361	0.012056	0.034522	0.012056	0.018305	0.004161	0.030361	0.004161
10-13	0.100884	0.18005	0.035641	*0.035641*	0.079166	0.136525	0.100884	*0.079166*
10-14	0.105484	0.226073	0.002405	0.002405	0.120589	0.107889	0.105484	***0.105484***
11-12	0.00727	0.010649	0.007036	0.007036	0.003379	0.000234	0.00727	0.000234
11-13	0.138515	0.202755	0.005917	0.005917	0.06424	0.132598	0.138515	0.06424
11-14	0.143115	0.248778	0.039153	*0.039153*	0.105663	0.103962	0.143115	*0.103962*
12-13	0.131245	0.192106	0.001119	0.001119	0.060861	0.132364	0.131245	0.060861
12-14	0.135845	0.126195	0.032117	***0.032117***	0.00965	0.103728	0.135845	0.00965
13-14	0.0046	0.046023	0.033236	0.0046	0.041423	0.028636	0.0046	0.0046
MAXIMUM	0.143115	0.248778	0.041558	0.039153	0.120589	0.136525	0.143115	0.105484

	Absolute difference between Arharrhiz Igourdane	Absolute difference between Arharrhiz Oussilkane	Absolute difference between Arharrhiz Bou Gafer	Minimum absolute difference for Arharrhiz	Absolute difference between Igourdane Oussilkane	Absolute difference between Igourdane Bou Gafer	Absolute difference between Igourdane Arharrhiz	Minimum absolute difference for Igourdane
10-11	0.018853	0.022705	0.014926	0.014926	0.041558	0.003927	39729.98507	0.003927
10-12	0.022466	0.012056	0.018305	0.012056	0.034522	0.004161	39760.9817	0.004161
10-13	0.215691	0.18005	0.079166	*0.079166*	0.035641	0.136525	39790.92083	*0.035641*
10-14	0.228478	0.226073	0.120589	***0.120589***	0.002405	0.107889	41517.87941	0.002405
11-12	0.003613	0.010649	0.003379	0.003379	0.007036	0.000234	39761.99662	0.000234
11-13	0.196838	0.202755	0.06424	0.06424	0.005917	0.132598	39791.93576	0.005917
11-14	0.209625	0.248778	0.105663	*0.105663*	0.039153	0.103962	41547.89434	*0.039153*
12-13	0.193225	0.192106	0.060861	0.060861	0.001119	0.132364	39792.93914	0.001119
12-14	0.094078	0.126195	0.00965	0.00965	0.032117	0.103728	41578.99035	0.032117
13-14	0.012787	0.046023	0.041423	0.012787	0.033236	0.028636	41608.95858	***0.028636***
MAXIMUM	0.228478	0.248778	0.120589	0.120589	0.041558	0.136525	41608.95858	0.039153

Note: Each cell of the absolute difference columns reports the value obtained from Equation 1 (see text). The last column for each pluton shows the minimum of these values and among them the three highest ones are italicized. The boldfaced values are related to the band pairs chosen for band couples of Figure 13.

full resolution (350–2500 nm) spectroradiometer and the Perkin Elmer lambda 19 spectrophotometer (350–2500 nm). For each sample the reflected radiation field was assumed to be Lambertian and the FieldSpec® reflectance was derived ex situ by rationing the average of four measurements to the radiance measured above a Spectralon panel. FieldSpec® data can be affected by the altered surface reflectance of the samples, which are often coated by desert varnish. For this reason the FieldSpec® data were compared to the corresponding Perkin Elmer signatures taken on the fresh rock surfaces (average of three measures) (Fig. 14). The comparison is also shown with the continuum removed to avoid the influence of the different environments during measurements and possible differences between the gain factors of the two instruments. Because the Arharrhiz granite is only slightly affected by the desert varnish coating, its signature has been derived from fresh rock samples only (Perkin-Elmer spectrometer).

The main difference between laboratory and field spectra can be attributed to the opaque minerals of the desert varnish that typically increase the spectral slope at lower wavelengths and mask absorption features at visible and near infrared rather than at higher wavelengths (e.g., Salisbury and D'Aria, 1992; Rivard et al., 1992, 1993) (Fig. 14A). In addition, the Bou Gafer FieldSpec® signatures, unlike the Perkin Elmer spectra, show characteristic shapes affected by hematite, which is particularly dominant in the desert varnish coating of this pluton (Fig. 14). Since hematite typically replaces pyroxenes in this granitoid, this may indicate that the opaque versus clay mineral content in the desert varnish can vary according to the mafic-feldspar modal ratios, and according to the original grade of alteration of the mafic minerals.

Laboratory signatures of all the studied granitoids show moderate absorptions at 1900 nm and 2208 nm caused by water and Al-OH, respectively, and related to the deuteric kaolinite from K-feldspar. The same features in FieldSpec® data are less marked, suggesting a minor overall contribution of clays to the desert varnish (Fig. 14B). The Mg-OH absorption typical of augite, hornblende, and biotite is more pronounced in both the FieldSpec® and laboratory signatures of the more mafic Oussilkane pluton. Similarly, the Oussilkane signatures show a minimum around 1000 nm, reflecting the contribution of augite and hornblende Fe crystal field effects (Fig. 14B).

The spectral signatures measured on rock samples were resampled to match the VNIR/SWIR ASTER bands and compared with spectral signatures derived from the 6S-corrected ASTER data (Fig. 15). The latter were collected from small training sites, called regions of interest (ROI), where the samples were collected. ASTER-derived signatures have similar trends with respect to the signatures of samples, but differences are still recognizable on the overall reflectance and the position of the absolute maximum. In particular, the ASTER signatures of the analyzed plutons reach their reflectance maxima in band 4, whereas in the FieldSpec® or Perkin-Elmer signatures, the maximum is sometimes shifted to band 5 (Fig. 15). Besides the fact that the procedure compares spectral data from a 15/30 by 15/30 m area with point measurements, the mismatch was probably due to the atmospheric correction of ASTER data, which was run with standard models not constrained by atmospheric parameters at the time of the satellite overpass. The correction was also run assuming flat surfaces and an average elevation for the entire scene. According to Sandmeier

(1995), horizontal visibility has to be known over the entire range of elevations within the test site, and in rugged terrain, such as that considered here, considerable modification in incoming irradiance can be observed.

Both sample spectra and the ASTER signatures of all plutons show a local minimum in band 6 due to Al-OH absorptions in this spectral range. However, the Oussilkane ASTER data are characterized by a lower increase in reflectance from band 6 to band 7 (Fig. 15). This particular feature is due to the mafic composition of the Oussilkane monzonite. The greater Mg-OH absorption of this body (Fig. 14) may be responsible for the lower reflectance in both bands 7 and 8. In addition, the Oussilkane monzonite spectra shows the lowest brightness because of its higher content of mafic minerals, whereas the Arharrhiz granite is characterized by the highest overall reflectance. These characteristics are the only distinctive features that can be recognized in both sample and ASTER signatures.

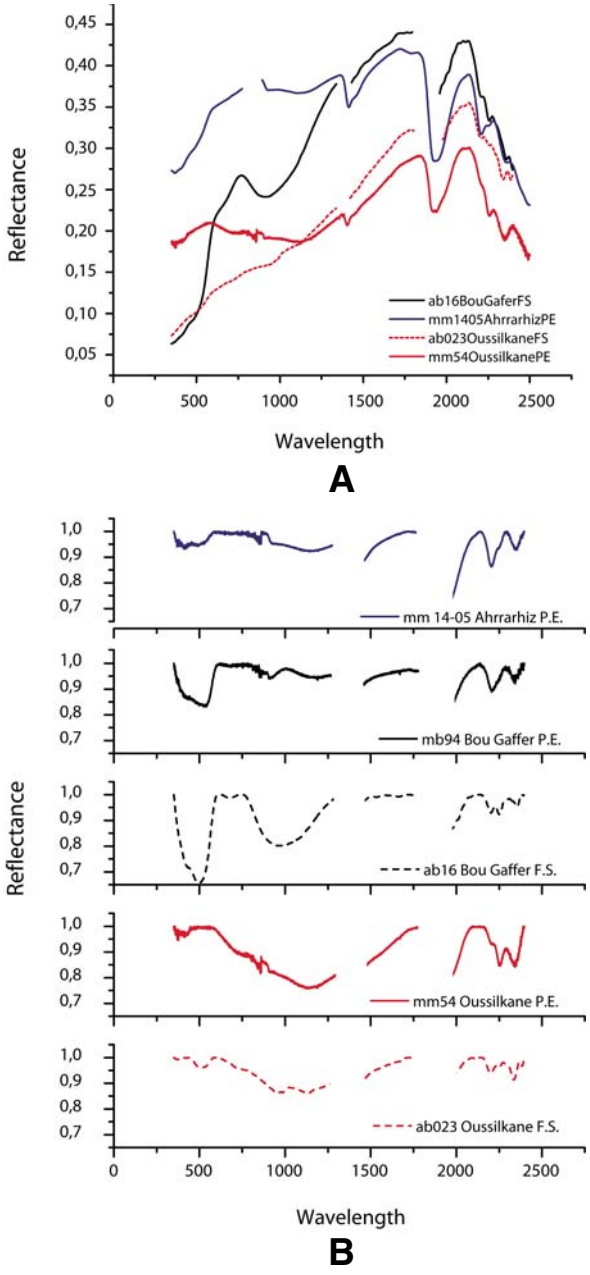

Figure 14. Full-resolution spectral signatures. (A) FieldSpec® (F.S.; see text) signatures of representative samples of Oussilkane monzonite and Bou Gafer quartz monzonite, and Perkin-Elmer (P.E.) signature of Arharrhiz granite sample (mm1405Ah). (B) Comparison between FieldSpec® and Perkin Elmer signatures of representative samples of Oussilkane monzonite, Bou Gafer quartz monzonite, and Arharrhiz granite (continuum removed).

False color composites and band ratios

To detect granitoids with similar compositions and map their intrusive boundaries, VNIR/SWIR false color and band ratios were selected according to the signature recorded by the spectroradiometric analysis or derived

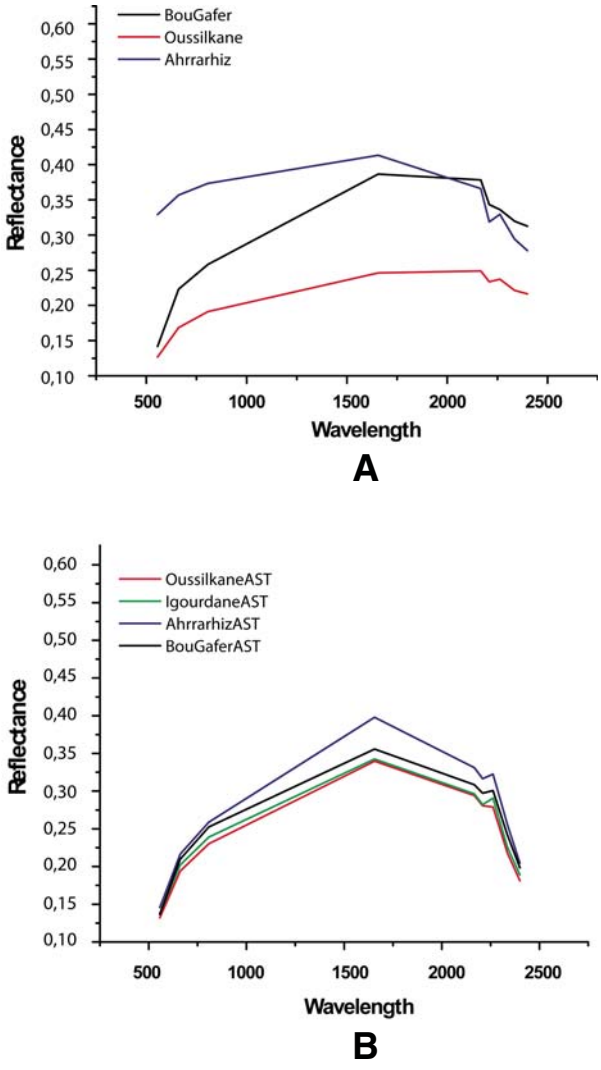

Figure 15. (A) Resampled spectral signatures of Oussilkane monzonite, Bou Gafer quartz monzonite, and Arharrhiz granite. (B) ASTER (AST—Advanced Spaceborne Thermal Emission and Reflection Radiometer) spectra of Oussilkane monzonite, Bou Gafer quartz monzonite, Arharrhiz and Igourdane granites (the regions of interest, ROIs, from which the signatures were derived are highlighted in Fig. 17).

from small training sites selected using the ASTER data. The RGB 9-4-1 color composition is effective for recognizing the high-K Ediacaran plutons (Fig. 16A). In particular, the Oussilkane pluton appears dark with highly variable colors, even though blue-green predominates. This reflects the low general albedo of this pluton, its significant lithological variability, and its low reflectance in band 9, possibly due to the Mg-OH absorptions. In contrast, the Arharrhiz granite is characterized by a higher overall reflectance and pink to cyan colors. These colors are due to both the significant contribution of band 4, which for this granite is the highest among the plutons considered (Fig. 15), and the lower level of absorption in band 1, probably due to the less widespread desert varnish coating. The Bou Gafer and Igourdane bodies show intermediate reflectance. In addition, the Bou Gafer quartz monzonite is characterized by large yellowish areas, possibly due to enhanced absorption in

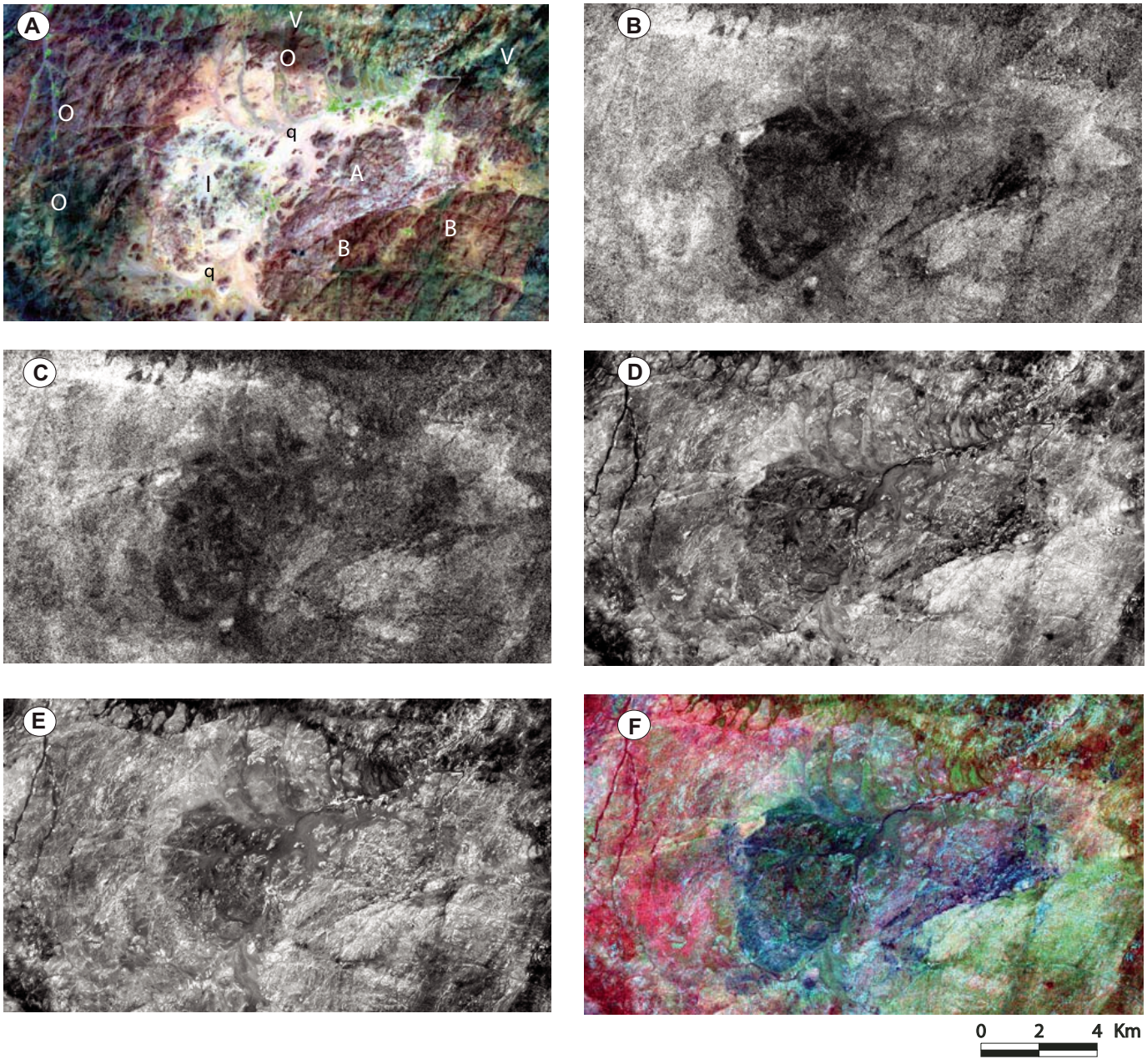

Figure 16. Detection of high-K plutons in the Oussilkane-Arharrhiz area (location in Fig. 1). (A) RGB (red-green-blue) false colors 9-4-1 composition (O—Oussilkane monzonite, A—Arharrhiz granite, B—Bou Gafer quartz monzonite, I—Igourdane granite, V—Ediacaran volcanites, q—Quaternary deposits). (B) Band ratio 6/7, in which the Oussilkane monzonite shows the highest gray values. (C) Band ratio 5/7, in which the Oussilkane monzonite shows the highest gray values. (D) Band ratio 6/1 in which the Bou Gafer quartz monzonite shows the highest gray values. (E) Band ratio 4/2, in which Arharrhiz granite shows the highest gray values. (F) RGB 5/7–6/1–4/2 color composite, in which all the high-K Ediacaran plutons are clearly recognizable (Oussilkane monzonite—red and magenta, Bou Gafer quartz monzonite—green and cyan, Arharrhiz granite—cyan and blue, Igourdane—dark blue).

band 1 (Fe oxides of the desert varnish, or as an alteration product of pyroxenes).

The choice of the ASTER band ratios used for the discrimination of these different granitoids was based on the signatures shown in Figure 15. From these signatures it is clear that the 7/6 ratio is very low for the Oussilkane monzonite (see also Fig. 16B). However, since no other distinctive features can be directly recognized in Figure 15B, the ratios were chosen on the same basis as the quantitative approach adopted for the thermal bands (see section on TIR data analysis). Following this calculation, the 5/7 ratio was selected for the Oussilkane monzonite (Table 3b; Fig. 16C), the 6/1 ratio for Bou Gafer quartz monzonite (Table 3b; Fig. 16D), the 4/2 ratio for the Arharrhiz granite (Table 3b; Fig. 16E), and the 6/2 ratio for the Igourdane granite (Table 3b). It is notable that the selected ratio for the Oussilkane monzonite is influenced by the Mg-OH absorptions (more mafic pluton), the ratio suited to the Bou Gafer quartz monzonite is in some way influenced by Al-OH and Fe charge transfer features (hydrothermal and surface alteration), and the ratio for the Arharrhiz granite reflects its higher reflectance, particularly in band 4. Because the Igourdane granite is well detected in all the above-mentioned ratios, the RGB 5/7–6/1–4/2 was chosen. In this false color composite the Oussilkane monzonite is dominated by red and magenta, the Bou Gafer quartz monzonite by green and yellow, the Arharrhiz granite by blue and cyan, and the Igourdane granite by dark blue (Fig. 16F).

Maximum likelihood and spectral angle mapper classifications

In order to refine the geological map of high-K Ediacaran intrusives, a maximum likelihood supervised classification (MLL) and a spectral angle mapper (SAM) classification were tested using the ASTER VNIR and SWIR bands. MLL regions of interest (ROI) were chosen on the basis of field observations and a petrographic analysis of rock samples collected during the campaign. In particular, the bedrock ROIs were limited to regions of confident lithological attribution, where petrographic samples were collected. Figure 17 shows training areas and the results of the classification compared with the geological map by Schiavo et al. (2007). Identification of the main lithological boundaries is straightforward, as it is the differentiation between plutons. In particular, the Arharrhiz and Igourdane granites are clearly delimited inside the Oussilkane and Bou Gafer plutons. In addition, the Arharrhiz granite surrounds the Igourdane body. The volcanic sequences, even if broadly differentiated, show more confused and scattered results. This is probably related to the fact that these series are characterized by an extreme lithological variability, in general due to frequent interleaving of andesites and/

TABLE 3B. SELECTION OF THE BAND COUPLES BEST SUITED FOR DISCRIMINATING THE EDIACARAN PLUTONS IN VNIR/SWIR

BAND COUPLE	Absolute difference between Oussilkane Bou Gafer	Absolute difference between Oussilkane Arharrhiz	Absolute difference between Oussilkane Igourdane	Minimum absolute difference for Oussilkane	Absolute difference between Bou Gafer Arharrhiz	Absolute difference between Bou Gafer Igourdane	Absolute difference between Bou Gafer Oussilkane	Minimum absolute difference for Bou Gafer
1-2	11.372659	8.921525	2.792324	2.792324	2.451134	8.580335	11.372659	2.451134
1-3	17.891083	15.152380	3.449062	3.449062	2.738703	14.442021	17.891083	2.738703
1-4	11.592755	44.691353	2.409185	2.409185	33.098598	14.001940	11.592755	*11.592755*
1-5	10.066882	23.701521	2.882532	2.882532	13.634639	12.949414	10.066882	10.066882
1-6	12.125225	22.249723	3.952357	3.952357	10.124498	16.077582	12.125225	***10.124498***
1-7	17.417470	30.143550	6.365302	*6.365302*	12.726080	11.052168	17.417470	*11.052168*
1-8	19.452597	24.422100	2.515582	2.515582	4.969503	16.937015	19.452597	4.969503
1-9	12.770377	9.804934	2.389192	2.389192	2.965443	10.381185	12.770377	2.965443
2-3	6.518424	6.230855	0.656738	0.656738	0.287569	5.861686	6.518424	0.287569
2-4	0.220096	35.769828	5.201509	0.220096	35.549732	5.421605	0.220096	0.220096
2-5	1.305777	14.779996	5.674856	1.305777	16.085773	4.369079	1.305777	1.305777
2-6	0.752566	13.328198	6.744681	0.752566	12.575632	7.497247	0.752566	0.752566
2-7	6.044811	21.222025	3.572978	3.572978	15.177214	2.471833	6.044811	2.471833
2-8	8.079938	15.500575	0.276742	0.276742	7.420637	8.356680	8.079938	7.420637
2-9	1.397718	0.883409	0.403132	0.403132	0.514309	1.800850	1.397718	0.514309
3-4	6.298328	29.538973	5.858247	5.858247	35.837301	0.440081	6.298328	0.440081
3-5	7.824201	8.549141	6.331594	*6.331594*	16.373342	1.492607	7.824201	1.492607
3-6	5.765858	7.097343	7.401419	5.765858	12.863201	1.635561	5.765858	1.635561
3-7	0.473613	14.991170	2.916240	0.473613	15.464783	3.389853	0.473613	0.473613
3-8	1.561514	9.269720	0.933480	0.933480	7.708206	2.494994	1.561514	1.561514
3-9	5.120706	5.347446	1.059870	1.059870	0.226740	4.060836	5.120706	0.226740
4-5	1.525873	20.989832	0.473347	0.473347	19.463959	1.052526	1.525873	1.052526
4-6	0.532470	22.441630	1.543172	0.532470	22.974100	2.075642	0.532470	0.532470
4-7	5.824715	14.547803	8.774487	5.824715	20.372518	2.949772	5.824715	2.949772
4-8	7.859842	20.269253	4.924767	4.924767	28.129095	2.935075	7.859842	2.935075
4-9	1.177622	34.886419	4.798377	1.177622	36.064041	3.620755	1.177622	1.177622
5-6	2.058343	1.451798	1.069825	1.069825	3.510141	3.128168	2.058343	2.058343
5-7	7.350588	6.442029	9.247834	***6.442029***	0.908559	1.897246	7.350588	0.908559
5-8	9.385715	0.720579	5.398114	0.720579	8.665136	3.987601	9.385715	3.987601
5-9	2.703495	13.896587	5.271724	2.703495	16.600082	2.568229	2.703495	2.568229
6-7	1.725281	4.326863	6.750695	1.725281	2.601582	5.025414	1.725281	1.725281
6-8	7.327372	2.172377	6.467939	2.172377	5.154995	0.859433	7.327372	0.859433
6-9	0.645152	12.444789	6.341549	0.645152	13.089941	5.696397	0.645152	0.645152
7-8	2.035127	5.721450	3.849720	2.035127	7.756577	5.884847	2.035127	2.035127
7-9	4.647093	20.338616	3.976110	3.976110	15.691523	0.670983	4.647093	0.670983
8-9	6.682220	14.617166	0.126390	0.126390	7.934946	6.555830	6.682220	6.555830
MAXIMUM	19.452597	44.691353	9.247834	6.442029	36.064041	16.937015	19.452597	11.592755

(continued)

TABLE 3B. SELECTION OF THE BAND COUPLES BEST SUITED FOR DISCRIMINATING THE EDIACARAN PLUTONS IN VNIR/SWIR (*continued*)

BAND COUPLE	Absolute difference between Arharrhiz Igourdane	Absolute difference between Arharrhiz Oussilkane	Absolute difference between Arharrhiz Bou Gafer	Minimum absolute difference for Arharrhiz	Absolute difference between Igourdane Oussilkane	Absolute difference between Igourdane Bou Gafer	Absolute difference between Igourdane Arharrhiz	Minimum absolute difference for Igourdane
1-2	6.129201	8.921525	2.451134	2.451134	2.792324	8.580335	6.129201	2.792324
1-3	11.703318	15.152380	2.738703	2.738703	3.449062	14.442021	11.703318	3.449062
1-4	47.100538	44.691353	33.098598	*33.098598*	2.409185	14.001940	47.100538	2.409185
1-5	26.584053	23.701521	13.634639	13.634639	2.882532	12.949414	26.584053	2.882532
1-6	26.202080	22.249723	10.124498	10.124498	3.952357	16.077582	26.202080	3.952357
1-7	23.778248	30.143550	12.726080	12.726080	6.365302	11.052168	23.778248	*6.365302*
1-8	21.906518	24.422100	4.969503	4.969503	2.515582	16.937015	21.906518	2.515582
1-9	7.415742	9.804934	2.965443	2.965443	2.389192	10.381185	7.415742	2.389192
2-3	5.574117	6.230855	0.287569	0.287569	0.656738	5.861686	5.574117	0.656738
2-4	40.971337	35.769828	35.549732	***35.549732***	5.201509	5.421605	40.971337	5.201509
2-5	20.454852	14.779996	16.085773	14.779996	5.674856	4.369079	20.454852	4.369079
2-6	20.072879	13.328198	12.575632	12.575632	6.744681	7.497247	20.072879	*6.744681*
2-7	17.649047	21.222025	15.177214	15.177214	3.572978	2.471833	17.649047	2.471833
2-8	15.777317	15.500575	7.420637	7.420637	0.276742	8.356680	15.777317	0.276742
2-9	1.286541	0.883409	0.514309	0.514309	0.403132	1.800850	1.286541	0.403132
3-4	35.397220	29.538973	35.837301	29.538973	5.858247	0.440081	35.397220	0.440081
3-5	14.880735	8.549141	16.373342	8.549141	6.331594	1.492607	14.880735	1.492607
3-6	14.498762	7.097343	12.863201	7.097343	7.401419	1.635561	14.498762	1.635561
3-7	12.074930	14.991170	15.464783	12.074930	2.916240	3.389853	12.074930	2.916240
3-8	10.203200	9.269720	7.708206	7.708206	0.933480	2.494994	10.203200	0.933480
3-9	4.287576	5.347446	0.226740	0.226740	1.059870	4.060836	4.287576	1.059870
4-5	20.516485	20.989832	19.463959	19.463959	0.473347	1.052526	20.516485	0.473347
4-6	20.898458	22.441630	22.974100	20.898458	1.543172	2.075642	20.898458	1.543172
4-7	23.322290	14.547803	20.372518	14.547803	8.774487	2.949772	23.322290	2.949772
4-8	25.194020	20.269253	28.129095	20.269253	4.924767	2.935075	25.194020	2.935075
4-9	39.684796	34.886419	36.064041	*34.886419*	4.798377	3.620755	39.684796	3.620755
5-6	0.381973	1.451798	3.510141	0.381973	1.069825	3.128168	0.381973	0.381973
5-7	2.805805	6.442029	0.908559	0.908559	9.247834	1.897246	2.805805	1.897246
5-8	4.677535	0.720579	8.665136	0.720579	5.398114	3.987601	4.677535	3.987601
5-9	19.168311	13.896587	16.600082	13.896587	5.271724	2.568229	19.168311	2.568229
6-7	2.423832	4.326863	2.601582	2.423832	6.750695	5.025414	2.423832	2.423832
6-8	4.295562	2.172377	5.154995	2.172377	6.467939	0.859433	4.295562	0.859433
6-9	18.786338	12.444789	13.089941	12.444789	6.341549	5.696397	18.786338	*5.696397*
7-8	1.871730	5.721450	7.756577	1.871730	3.849720	5.884847	1.871730	1.871730
7-9	16.362506	20.338616	15.691523	15.691523	3.976110	0.670983	16.362506	0.670983
8-9	14.490776	14.617166	7.934946	7.934946	0.126390	6.555830	14.490776	0.126390
MAXIMUM	47.100538	44.691353	36.064041	35.549732	9.247834	16.937015	47.100538	6.744681

Note: Each cell of the absolute difference columns reports the value obtained from Equation 1 (see text). The last column for each pluton shows the minimum of these values and among them the three highest ones are italicized. The boldfaced values are related to the band pairs chosen for band couples of Figure 13.

or dacites in dominant rhyolites (e.g., Schiavo et al., 2007; Massironi et al., 2007), a widespread desert varnish coating, and very different degrees of hydrothermal alteration. The contact between the Ediacaran volcanic sequences and the Oussilkane pluton is locally underlined with pixels wrongly attributed to the Bou Gafer quartz monzonite. This effect is probably due to mixed pixels because in this area, talus deposits, derived from the cliffs of volcanic rocks, overlie the Oussilkane monzonites and may influence their reflectance.

SAM classification was attempted to detect different granitoid bodies using spectral signatures derived either from the ROIs or from FieldSpec® analyses (Fig. 18). In the first case the results are good and as useful as the MLL classification, although at higher angles Quaternary deposits are frequently attributed to the granitoid bodies (Figs. 18A, 18B); in the second case the results are weak and uninformative (Fig. 18C). This inadequate result is probably due to the inconsistency between satellite and sample reflectance values already mentioned and the ineffectiveness of SAM for discriminating between these rocks on the basis of their original spectral signatures using multispectral rather than hyperspectral data.

CONCLUSIONS

The remote sensing detection of granitoid rocks has been a persistent problem, particularly when the rocks are of similar composition and coated by desert varnish. In this work, the potential of ASTER data has been tested with this objective on the Jebel Saghro Precambrian basement (eastern Anti-Atlas, Morocco). The remote sensing approach was coupled with field observations and petrographic analyses, and was subdivided into two main steps.

In the first step, basic procedures, governed by petrographic knowledge of the studied rocks, were applied to atmospherically corrected and orthorectified ASTER data. Specifically, RGB 7-3-1, 4/8–2/1–4/3, and 4/6–2/1–4/3 false color composites, particularly sensitive to Fe and OH absorptions, were used to highlight the main contacts of different lithological units consisting of low-grade metasediments, calc-alkaline plutons, and complex volcanic sequences. In addition, the false color images based on the band ratios described above and principal components analysis calculated on VNIR and SWIR

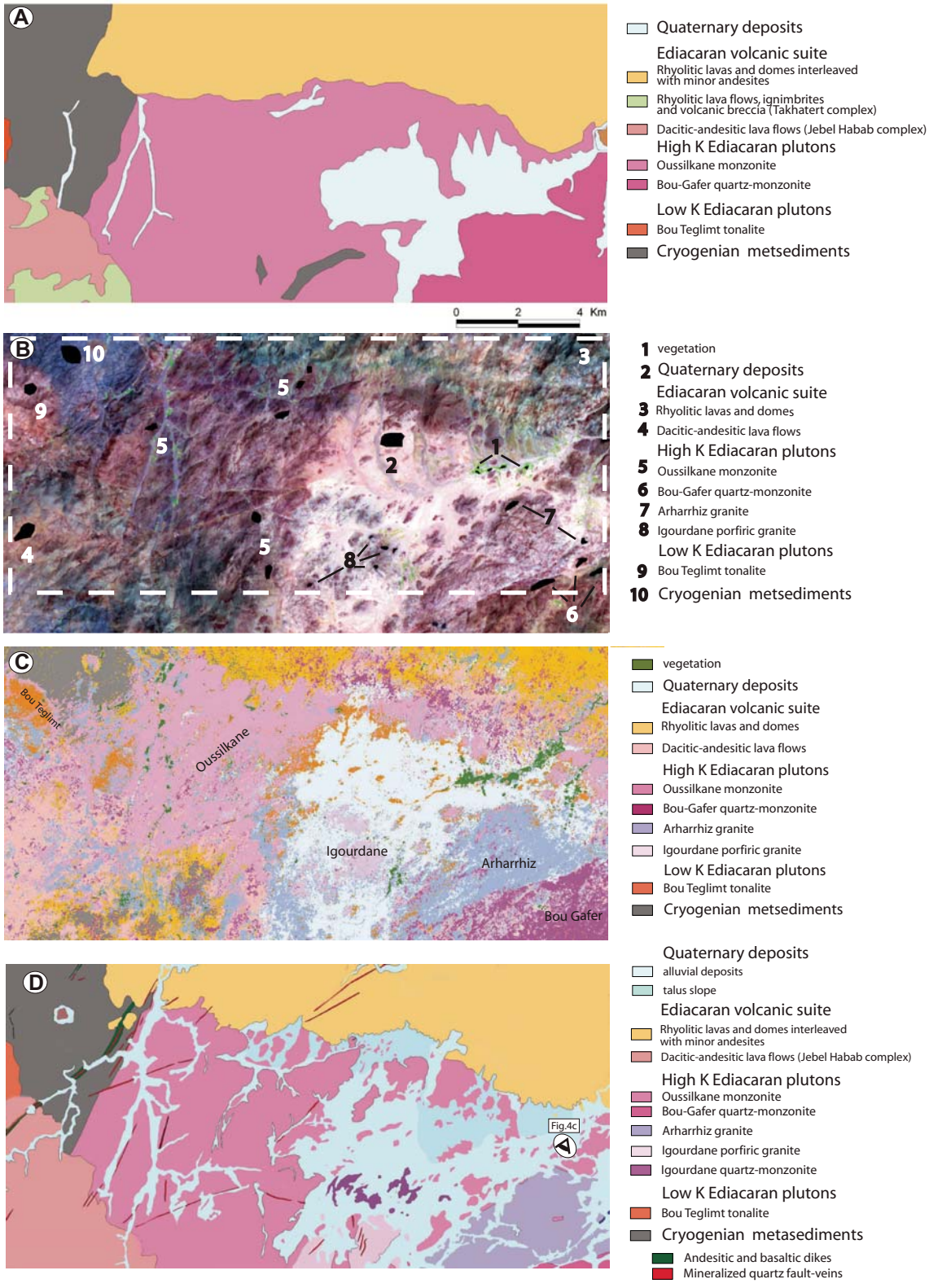

Figure 17. Maximum likelihood (MLL) supervised classification (location in Fig. 1). (A) Excerpt from the 1:200,000 geological map (redrawn after Hinderemeyer et al., 1977; Du Dresnay et al., 1988). (B) ASTER 731 false color composite with region of interest (ROI) used for the MLL classification (white square—boundaries of the geological map by Schiavo et al. [2007] displayed in Fig. 17D). (C) Results of MLL supervised classification: boundaries between Ediacaran volcaniclastic series, Cryogenian metasediments, and Ediacaran plutons are quite well defined. Ediacaran metasediments are particularly well delineated; the low-K pluton (Bou Teglimt tonalite) is distinguished from the high-K ones, and the Bou Gafer quartz monzonite (lower right corner), the Oussilkane pluton (main body), and Arharriz and Igourdane granites (center of the image) are clearly discriminated. The more disturbed boundaries between the Oussilkane monzonite and volcaniclastic complexes are due to Quaternary talus slope. (D) Geological map after Schiavo et al. (2007): an overall agreement with the classification is evident.

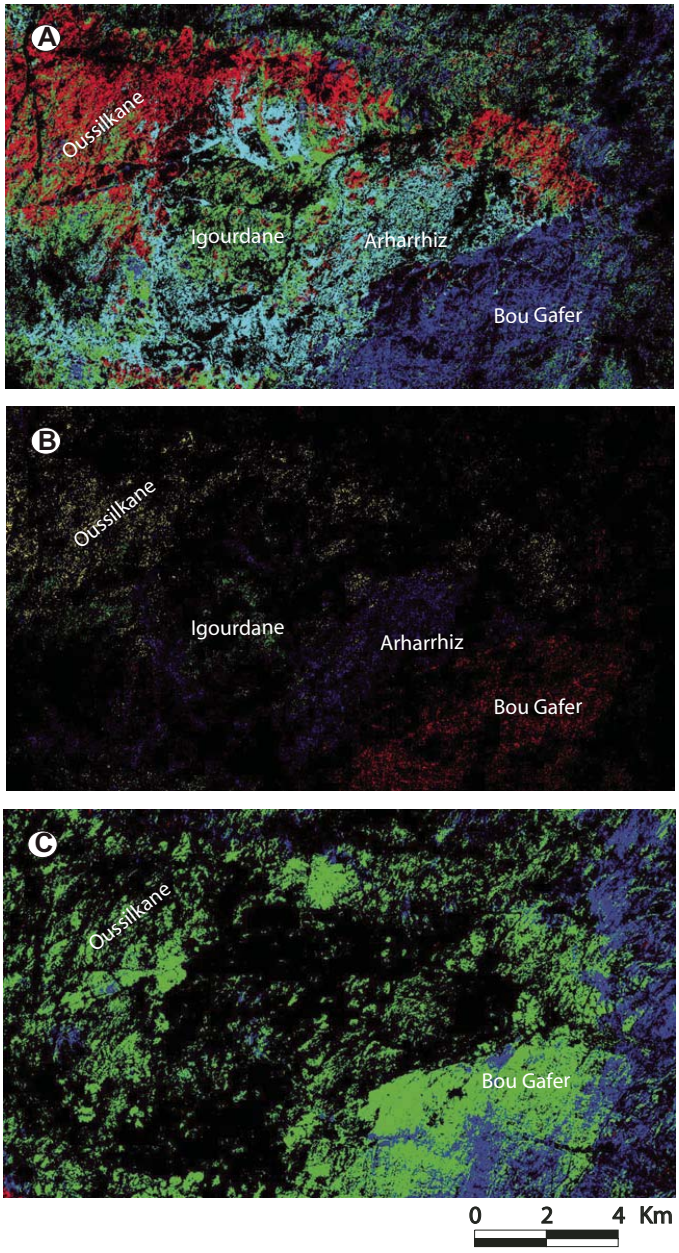

Figure 18. Spectral angle mapper (SAM) classification of high-K granitoids (location in Fig. 1). (A) SAM classification based on training area–derived signatures (maximum angle 0.02 radians). (B) SAM classification based on training area–derived signatures (maximum angle 0.01 radians). (C) SAM classification based on FieldSpec® (see text) signature of Bou Gafer quartz monzonite (green) and the Oussilkane pluton (blue) (maximum angle 0.02 radians); the results are ambiguous and do not highlight the boundaries between different plutons.

bands, were applied to emphasize Fe, OH, and S absorptions and thus ease the detection of mineralized veins, fault breccias, and related alteration halos.

During the second stage, a major effort was dedicated to distinguishing between confining high-K calc-alkaline plutons of Ediacaran age with slightly different compositions (Bou Gafer quartz monzonite, Oussilkane monzonite, Arharrhiz and Igourdane granites). Both TIR and VNIR/SWIR data were considered suitable to achieve this. In particular, a decorrelation stretch of RGB false color composites, created with 14–13–10 TIR bands and 14/12–14/10–13/14 band ratios, was effective in highlighting Reststrahlen and Christiansen features of the granitoids with different silica contents (primarily the Oussilkane monzonite and the Arharrhiz granites, secondarily the Bou Gafer quartz monzonite and Igourdane granite). The TIR band ratios were selected using a quantitative analysis of the spectral signatures derived directly from ASTER data in sites of well-constrained lithology. Concerning VNIR/SWIR wavelengths, a comparison between spectra directly derived from the ASTER image and signatures acquired on samples of the plutons has highlighted some common features. However, these are not sufficient to justify a direct use of FieldSpec® signatures during image processing. For this reason, as for the TIR data, VNIR/SWIR band ratios were selected on the basis of a quantitative analysis of the ASTER derived spectra, and the RGB 5/7–6/1–4/9 color composite was specifically selected to highlight the high-K calc-alkaline plutons.

Finally, classifications focusing on the same Ediacaran granitoids were attempted using the VNIR/SWIR bands. In particular, an MLL based on small ROIs constrained through field and petrographic analyses was implemented and compared with a SAM classification based upon rock signatures derived from FieldSpec® data and ROIs. The MLL and SAM classifications based on ROIs signatures gave good results, but the SAM classification realized through the FieldSpec® signatures was useless, because of the mismatch between satellite and sample reflectance values.

The main findings of our remote sensing analysis can be summarized as follows.

1. The potential of ASTER data for geological mapping of basement rocks has been further demonstrated, with particular regard to granitoids. In particular, the approach adopted here, consisting in the detection of the main geological boundaries followed by discrimination between granitoids, is particularly effective.

2. Integrated analysis of both TIR and VNIR/SWIR data is of paramount importance for mapping plutonic bodies. It is well known that ASTER thermal bands are useful for discriminating granitoids with different silica content, but in the case of plutonic bodies of similar composition, such as those studied on the Saghro massif, the VNIR/SWIR bands can give even more effective results. Indeed, these wavelengths are affected by both the original content of mafic minerals (Fe, Mg-OH absorptions) and the degree of hydrothermal and surface alteration. These last two properties, generally considered to be impediments to the lithological detection of granitoid rocks, can instead be very useful because the first may directly depend on the magmatic evolution of a plutonic body, and the second depends on its textural character and may be indirectly related to its modal ratio.
3. The spectral signatures derived from ASTER data using regions of very confident lithological attribution are self-consistent, can directly drive the processing (false color composites and band ratios), and can be successfully integrated into the SAM classification. In contrast, the signatures derived from spectrophotometric analysis of samples can be used only as qualitative references, if ASTER data are corrected only by cross-talk calibration and standard atmospheric models unconstrained by atmospheric parameters at the time of the satellite overpass (specific processing steps such as those proposed by Rowan et al. [2003] are needed).
4. When a limited number of confining units are being studied, a quantitative approach based on reliable ASTER-derived signatures can be used to assess the potential of each band couple for discriminating a defined unit. In particular, the absolute differences between bands were calculated and compared among the analyzed granitoids in order to detect the band ratios more effective in discriminating specific plutons (see discussion on remote sensing detection of the Ediacaran plutons and Tables 3a and 3b).
5. The MLL classification can be even more effective than the SAM classification if it is based on training areas well constrained by means of field observations and petrographic analyses.

ACKNOWLEDGMENTS

We thank two anonymous reviewers and associate editor Francesco Mazzarini, who greatly improved the manuscript with their suggestions. Simon Crowhurst is acknowledged for the revision of the English text. Funding for this research was provided by the Ministère de l'Energie et des Mines du Maroc within the geological mapping project of the Saghro massif and by the University of Padova through the ex 60% grant to M.M.

REFERENCES CITED

Abrams, M., 2000, The Advanced Spaceborne Thermal Emission and Reflection Radiometer (ASTER): Data products for the high spatial resolution imager on NASA's Terra platform: International Journal of Remote Sensing, v. 21, p. 847–859, doi: 10.1080/014311600210326.

Baroudi, Z., El Beraaouz, H., Rahimi, A., Saquaque, A., and Chouhaidi, M.Y., 1999, Minéralisation polymétalliques argentifères d'Imiter (Jbel Saghro, Anti-Atlas, Maroc): Minéralogie, évolution des fluides minéralisateurs et mécanismes de depot: Chronique des Mines et de Recherche Minière, v. 536–537, p. 91–112.

Boyer, C., Chikhaoui, M., Dupuy, C., and Leblanc, M., 1978, Le volcanisme calco-alcalin précambrien terminal de l'Anti-Atlas (Maroc) et ses alterations: Interprétation géodynamique: Paris, Académie des Sciences Comptes Rendus, v. 287, p. 427–430.

Cheilletz, A., Levresse, G., Gasquet, D., Aziz Samir, M.R., Zyadi, R., Archibald, D.A., and Farrar, E., 2002, The giant Imiter silver deposit: Neoproterozoic epithermal mineralization in the Anti Atlas, Morocco: Mineralium Deposita, v. 37, p. 772–781, doi: 10.1007/s00126-002-0317-0.

Choubert, G., 1945, Sur le Précambrien marocain: Paris, Académie des Sciences Comptes Rendus, v. 9, p. 249–251.

Choubert, G., 1952, Le Précambrien III et le Géorgien de l'Anti-Atlas: Introduction stratigraphique, *in* Hupé, P., ed., Contribution à l'étude du Cambrien inférieur et Précambrien III de l'Anti-Atlas marocain: Notes et Mémoires Service Géologique Maroc, v. 103, p. 17–39.

Christensen, P.R., and Harrison, S.T., 1993, Thermal Infrared emission spectroscopy of natural surfaces: Application to desert varnish coatings on rocks: Journal of Geophysical Research, v. 98, p. 19,819–19,834, doi: 10.1029/93JB00135.

Clark, R.N., King, T.V.V., Klejwa, M., Swayze, G.A., and Vergo, N., 1990, High spectral resolution reflectance spectroscopy of minerals: Journal of Geophysical Research, v. 95, no. B8, p. 12,653–12,680, doi: 10.1029/JB095iB08p12653.

Crowley, J.K., Brickley, D.W., and Rowan, L.C., 1989, Airbone imaging spectrometer data of the Ruby Mountains, Montana: Mineral discrimination using relative absorption band-depth images: Remote Sensing of Environment, v. 29, p. 121–134, doi: 10.1016/0034-4257(89)90021-7.

Dal Piaz, G.V., Malusà, M., Eddebbi, A., El Boukhari, A., Ellero, A., Laftouhi, N., Massironi, M., Ouanaimi, H., Pertusati, P.C., Polino, R., Schiavo, A., Taj-Eddine, K., and Visonà, D., 2007, Carte Géologique du Maroc au 1/50 000, feuille Taghazout– Notice explicative: Notes et Mémoires Service Géologique Maroc, v. 519, 69 p.

De Wall, H., Kober, B., Errami, E., Ennih, N., and Greiling, R.O., 2001, Age de mise en place et contexte géologique des granitoïdes de la boutonnière d'Imiter (Saghro oriental, Anti-Atlas, Maroc): 2ème Colloque International: Marrakech, Magmatisme, Métamorphisme et Minéralisations Associées, v. 10–12, p. 19.

Dorn, R.L., and Oberlander, T.M., 1981, Microbial origin of desert varnish: Science, v. 213, p. 1245–1247, doi: 10.1126/science.213.4513.1245.

Drury, S.A., 1997, Image interpretation in geology: London, Chapman and Hall, 283 p.

Du Dresnay, R., Hindermeyer, J., Emberger, A., Caia, J., Destombes, J., and Hollard, H., 1988, Carte géologique du Maroc: Todrha-Ma'der (Anti-Atlas oriental, sones axiale et péripherique Nord et Sud) au 1:200.000: Notes et Mémoires Service Géologique Maroc, v. 243.

El Boukhari, A., Chaabane, A., Rocci, G., and Tane, J.L., 1992, Upper Proterozoic ophiolites of the Siroua massif (Anti-Atlas Morocco), a marginal sea and transform fault system: Journal of African Earth Sciences, v. 14, p. 67–80, doi: 10.1016/0899-5362(92)90056-I.

El Boukhari, A., Musumeci, G., Algouti, A., Cerrina Feroni, A., Ghiselli, F., Ottria, G., Ouanaimi, H., Pertusati, P.C., Taj-Eddine, K., and Visonà, D., 2007, Carte Géologique du Maroc au 1/50 000, feuille Imi n'Ouzrou—Notice explicative: Notes et Mémoires Service Géologique Maroc, v. 517, 72 p.

Ennih, N., and Liégeois, J.P., 2001, The Moroccan Anti-Atlas: The West African craton passive margin with limited Pan-African activity: Implication for the northern limit of the craton: Precambrian Research, v. 112, p. 289–302, doi: 10.1016/S0301-9268(01)00195-4.

Errami, E., De Wall, H., and Greiling, R.O., 1999, Preliminary results of pan-African granitoid emplacement studies in the East Saghro (Anti-Atlas, Morocco) using the AMS method, *in* de Wall, H., and Greiling, R.O., eds., Aspects of Pan-African tectonics: lnternational Bureau Eorschungszentrum, Jùlich, Scientific series, v. 32, p. 37–44.

Fekkak, A., Pouclet, A., Ouguir, H., Ouazzani, H., Badra, L., and Gasquet, D., 2001, Géochimie et signification géotectonique des volcanites du Cryogénien inférieur du Saghro (Anti-Atlas oriental, Maroc): Geodinamica Acta, v. 14, p. 373–385, doi: 10.1016/S0985-3111(01)01073-7.

Hefferan, K.P., Karson, J.A., and Saquaque, A., 1992, Proterozoic collisional basin in a Pan-African suture zone, Anti-Atlas mountains, Morocco: Precambrian Research, v. 54, p. 295–319, doi: 10.1016/0301-9268(92)90075-Y.

Hefferan, K.P., Admou, H., Karson, J.A., and Saquaque, A., 2000, Anti-Atlas (Morocco) role in Neoproterozoic Western Gondwana reconstruction: Precambrian Research, v. 103, p. 89–96, doi: 10.1016/S0301-9268(00)00078-4.

Hefferan, K.P., Admou, H., Hilal, R., Karson, J.A., Saquaque, A., Juteau, T., Bohn, M.M., Samson, S.D., and Kornprobst, J.M., 2002, Proterozoic blueschist-bearing melange in the Anti-Atlas Mountains, Morocco: Precambrian Research, v. 118, p. 179–194, doi: 10.1016/S0301-9268(02)00109-2.

Hewson, R.D., Cudahy, T.J., Mizuhiko, S., Ueda, K., and Mauger, A.J., 2005, Seamless geological map generation using ASTER in the Broken Hill–Curnamona province of Australia: Remote Sensing of Environment, v. 99, p. 159–172, doi: 10.1016/j.rse.2005.04.025.

Hinderemeyer, J., 1953, Le Précambrien III du Sarho: Paris, Académie des Sciences Comptes Rendus, v. 237, p. 1024–1026.

Hinderemeyer, J., Gauthier, H., Destombes, J., and Choubert, G., 1977, Carte géologique du Maroc, Jbel Saghro-Dades (Haut-Atlas central, sillon sud-atlasique et Anti-Atlas oriental) au 1:200000: Notes et Mémoires Service Géologique Maroc, v. 161.

Hook, S.J., Abbott, E.A., Grove, C., Kahle, A.B., and Palluconi, F., 1999, Use of multispectral thermal infrared data in geological studies, *in* Rencz, A.N., ed., Remote sensing for the Earth sciences: Manual of remote sensing, Volume 3: New York, John Wiley and Sons, p. 59–103.

Hooke, R.L., Yang, H.Y., and Weiblen, P.W., 1969, Desert varnish: An electron probe study: Journal of Geology, v. 77, p. 275–288.

Hubbard, B.E., and Crowley, J.K., 2005, Mineral mapping on Chilean-Bolivian Altipiano using co-orbital ALI, ASTER and Hyperion imagery: Data dimensionality issues and solutions: Remote Sensing of Environment, v. 99, p. 173–186, doi: 10.1016/j.rse.2005.04.027.

Hubbard, B.E., Rowan, L.C., Dusel-Bacon, C., and Eppinger, R.G., 2007, Geological mapping and mineral resource assessment of the Healy and Talkeetna mountains quadrangles, Alaska using minimal cloud and snow cover ASTER data: U.S. Geological Survey Open-File Report 2007–1046, 18 p.

Hunt, G.R., 1980, Electromagnetic radiation: The communication link in remote sensing, *in* Siegal, B.S., and Gillespie, R., eds., Remote sensing in geology: New York, Wiley, p. 5–45.

Ighid, L., Saquaque, A., and Reuber, I., 1989, Syn-kinematic plutons and the major panafrican deformation in the eastern Saghro (Imiter, Anti-Atlas, Morocco): Paris, Académie des Sciences Comptes Rendus, v. 309, p. 615–620.

Lang, H.R., 1999, Stratigraphy, *in* Rencz, A.N., ed., Remote sensing for the Earth sciences: Manual of remote sensing, Volume 3: New York, John Wiley and Sons, p. 357–374.

Leblanc, M., and Lancelot, J.R., 1980, Interprétation géodinamique du domaine pan-africain (Précambrien terminal) de l'Anti-Atlas (Maroc) à partir de données géologiques et géochronologiques: Canadian Journal of Earth Sciences, v. 17, p. 142–155.

Leistel, J.M., and Quadrouci, A., 1991, Le gisement argentifère d'Imiter (Protérozoïque supérieur de l'Anti-Atlas, Maroc), Contrôle des minéralisation, hypothèse et perspective pour l'exploitation: Chronique des Mines et de Recherche Minière, v. 502, p. 5–22.

Levresse, G., Cheilletz, A., Gasquet, D., Reisberg, L., Deloulea, E., Martya, B., and Kyserc, K., 2004, Osmium, sulphur, and helium isotopic results from the giant Neoproterozoic epithermal Imiter silver deposit, Morocco: Evidence for a mantle source: Chemical Geology, v. 207, p. 59–79, doi: 10.1016/j.chemgeo.2004.02.004.

Longhi, I., Sgavetti, M., Chiari, R., and Mazzoli, C., 2001, Spectral analysis and classification of metamorphic rocks from reflectance spectra in the 0.4–2.5 um interval: A tool for hyperspectral data interpretation: International Journal of Remote Sensing, v. 22, p. 3763–3782, doi: 10.1080/01431160010006980.

Malusà, M.G., Polino, R., Feroni, A.C., Ellero, A., Otaria, G., Baidder, L., and Musumeci, G., 2007, Post-Variscan tectonics in eastern Anti-Atlas (Morocco): Terra Nova, v. 19, p. 481–489, doi: 10.1111/j.1365-3121.2007.00775.x.

Mars, J.C., and Rowan, L.C., 2006, Regional mapping of phyllic and argillic-altered rocks in the Zagros magmatic arc, Iran, using Advanced Spaceborne Thermal Emission and Reflection Radiometer (ASTER), data and logical operator algorithms: Geosphere, v. 2, no. 3, p. 161–186, doi: 10.1130/GES00044.1.

Massironi, M., Moratti, G., Algouti, A., Benvenuti, M., Dal Piaz, G.V., Eddebbi, A., El Boukhari, A., Laftouhi, N., Ouanaimi, H., Schiavo, A., Taj-Eddine, K., and Visonà D., 2007, Carte Géologique du Maroc au 1/50 000, feuille Boumalne—Notice explicative: Notes et Mémoires Service Géologique Maroc, v. 521, 80 p.

Mifdal, A., and Peucat, J.J., 1986, Datation U-Pb et Rb-Sr du volcanisme acide du Précambrien marocain et du socle sous-jacent dans la région de Ouarzazate: Apport au problème de la limite Précambrien-Cambrien: Sciences Géologiques (Bulletin), v. 38, p. 185–200.

Ouguir, H., Macaudiere, J., Dagallier, G., Qadrouci, A., and Leistel, J.M., 1994, Structural framework of the Ag-Hg deposit of Imiter (Anti-Atlas, Morocco): Metallogenic inferences: Bulletin de la Société Géologique de France, v. 165, p. 233–248.

Potter, R.M., and Rossman, G.R., 1977, Desert varnish: The importance of clay minerals: Science, v. 196, p. 1446–1448, doi: 10.1126/science.196.4297.1446.

Potter, R.M., and Rossman, G.R., 1979, The manganese- and iron-oxide mineralogy of desert varnish: Chemical Geology, v. 25, no. 1-2, p. 79–94, doi: 10.1016/0009-2541(79)90085-8.

Rivard, B., Arvidson, R.E., Duncan, I.J., Sultan, M., and El Kaliouby, B., 1992, Varnish, sediment, and rock controls on the spectral reflectance of outcrops in arid regions: Geology, v. 20, p. 295–298, doi: 10.1130/0091-7613(1992)020<0295:VSARCO>2.3.CO;2.

Rivard, B., Petroy, S.B., and Miller, J.R., 1993, Measured effects of desert varnish on the mid-infrared spectra of weathered rocks as an aid to TIMS imagery interpretation: IEEE Transactions on Geoscience and Remote Sensing, v. 31, no. 1, p. 284–291, doi: 10.1109/36.210468.

Rowan, L.C., and Mars, J.C., 2003, Lithological mapping in the Mountain Pass, California area using Advanced Spaceborne Thermal Emission and Reflection Radiometer (ASTER) data: Remote Sensing of Environment, v. 84, p. 350–366, doi: 10.1016/S0034-4257(02)00127-X.

Rowan, L.C., Crowley, J.K., Schmidt, R.G., Ager, C.M., and Mars, J.C., 2000, Mapping hydrothermally altered rocks by analyzing hyperspectral image (AVIRIS) data of forested areas in the southeastern United States: Journal of Geochemical Exploration, v. 68, no. 3, p. 145–166, doi: 10.1016/S0375-6742(99)00081-3.

Rowan, L.C., Hook, S.J., Abrams, M.J., and Mars, J.C., 2003, Mapping hydrothermally altered rocks at Cuprite, Nevada, using the Advanced Spaceborne Thermal Emission and Reflection Radiometer (ASTER), A new satellite-imaging system: Economic Geology and the Bulletin of the Society of Economic Geologists, v. 98, p. 1019–1027.

Rowan, L.C., Mars, J.C., and Simpson, C.J., 2005, Lithologic mapping of the Mordor, NT, Australia ultramafic complex by using the Advanced Spaceborne Thermal Emission and Reflection Radiometer (ASTER): Remote Sensing of Environment, v. 99, p. 105–126, doi: 10.1016/j.rse.2004.11.021.

Rowan, L.C., Schmidt, R.G., and Mars, J.C., 2006, Distribution of hydrothermally altered rock in the Reko Diq, Pakistan mineralized area based on spectral analysis of ASTER data: Remote Sensing of Environment, v. 104, p. 74–87, doi: 10.1016/j.rse.2006.05.014.

Sabins, F., 1996, Remote sensing: Principles and interpretation: New York, Freeman and Co., 494 p.

Sabine, C.V., Realmuto, V.J., and Taranik, J.V., 1994, Quantitative estimation of granitoid composition from thermal infrared multispectral scanner (TIMS) data, Desolation Wilderness, northern Sierra Nevada, California: Journal of Geophysical Research, v. 99, p. 4261–4271, doi: 10.1029/93JB03127.

Salisbury, J.W., and D'Aria, D.M., 1992, Emissivity of terrestrial material in the 8–14 μm atmospheric window: Remote Sensing of Environment, v. 42, p. 83–106, doi: 10.1016/0034-4257(92)90092-X.

Sandmeier, R.S., 1995, A physically-based radiometric correction model: Correction of atmospheric effects in optical satellite data of rugged terrain [Ph.D. thesis]: Department of Geography, University of Zurich, Remote Sensing Laboratories, Remote Sensing Series, v. 26, 110 p.

Saquaque, A., Admou, H., Karson, J.A., Hefferan, J., and Reuber, I., 1989, Precambrian accretionary tectonics in the Bou Azzer El Graara region, Anti-Atlas, Morocco: Geology, v. 17, p. 1107–1110, doi: 10.1130/0091-7613(1989)017<1107:PATITB>2.3.CO;2.

Saquaque, A., Benharref, M., Abia, H., Mrini, Z., Reuber, I., and Karson, J.A., 1992, Evidence for a Panafrican volcanic arc and wrench fault tectonics in the Jbel Saghro, Anti Atlas, Morocco: Geologische Rundschau, v. 81, p. 1–13, doi: 10.1007/BF01764536.

Schiavo, A., and Taj-Eddine, K., Algouti, Ah., Benvenuti, M., Dal Piaz, G.V., Eddebbi, A., El Boukhari, A., Laftouhi, N., Massironi, M., Moratti, G., Ouanaimi, H., Pasquarè, G., and Visonà, D., 2007, Carte Géologique du Maroc au 1/50 000, feuille Imtir—Notice explicative: Notes et Mémoires Service Géologique Maroc, v. 518, 96 p.

Sgavetti, M., Ferrari, M.C., Chiari, P., Fantozzi, L., and Longhi, I., 1995, Stratigraphic correlation by integrating photostratigraphy and remote sensing multispectral data: An example from Jurassic-Eocene strata, northern Somalia: American Association of Petroleum Geologists Bulletin, v. 79, p. 1571–1589.

Thomas, R.J., Fekkak, A., Ennih, N., Errami, E., Loughlin, S.C., Gresse, P.G., Chevallier, L.P., and Liégeois, J.-P., 2004, A new lithostratigraphic framework for the Anti-Atlas Orogen, Morocco: Journal of African Earth Sciences, v. 39, no. 3-5, p. 217–226, doi: 10.1016/j.jafrearsci.2004.07.046.

Van Ruitenbeek, F.J.A., Debba, P., Van Der Meer, F.D., Cudahy, T., Van Der Meijde, M., and Hale, M., 2006, Mapping white micas and their absorption wavelengths using hyperspectral band ratios: International Journal of Remote Sensing, v. 18, p. 1245–1257.

Vermote, E.F., Tanrè, D., Deizè, J.L., Herman, M., and Morcrette, J.J., 1997, Second simulation of the satellite signal in the solar spectrum (6S): An overview: IEEE Transactions on Geoscience and Remote Sensing, v. 35, p. 675–686, doi: 10.1109/36.581987.

Watts, D.R., Harris, N.B., and the NASA GLENN SOARS Working Group, 2005, Mapping granite and gneiss in domes along the North Hymalayan antiform with ASTER SWIR band ratios: Geological Society of America Bulletin, v. 117, p. 879–886, doi: 10.1130/B25592.1.

Yamaguchi, Y., Kahle, A.B., Tsu, H., Kawakami, T., and Pniel, M., 1998, Overview of Advanced Spaceborne Thermal Emission and Reflection Radiometer (ASTER): IEEE Transactions on Geoscience and Remote Sensing, v. 36, p. 1062–1071, doi: 10.1109/36.700991.

Manuscript Received 8 September 2007
Revised Manuscript Received 30 March 2008
Manuscript Accepted 14 April 2008